

Rest-Frame Optical Spectroscopy of Ten $z \sim 2$ Weak Emission-Line Quasars

Y. CHEN,^{1,2} B. LUO,^{1,2} W. N. BRANDT,^{3,4,5} WENWEN ZUO,⁶ COOPER DIX,^{7,8} TRUNG HA,⁷ BRANDON MATTHEWS,⁷
JEREMIAH D. PAUL,⁹ RICHARD M. PLOTKIN,^{9,10} AND OHAD SHEMMER⁷

¹*School of Astronomy and Space Science, Nanjing University, Nanjing, Jiangsu 210093, China*

²*Key Laboratory of Modern Astronomy and Astrophysics (Nanjing University), Ministry of Education, Nanjing 210093, China*

³*Department of Astronomy & Astrophysics, 525 Davey Lab, The Pennsylvania State University, University Park, PA 16802, USA*

⁴*Institute for Gravitation and the Cosmos, The Pennsylvania State University, University Park, PA 16802, USA*

⁵*Department of Physics, 104 Davey Lab, The Pennsylvania State University, University Park, PA 16802, USA*

⁶*Shanghai Astronomical Observatory, Chinese Academy of Sciences, 80 Nandan Road, Shanghai 200030, China*

⁷*Department of Physics, University of North Texas, Denton, TX, 76203, USA*

⁸*Department of Astronomy, The University of Texas at Austin, Austin, TX 78712, USA*

⁹*Department of Physics, University of Nevada, Reno, NV 89557, USA*

¹⁰*Nevada Center for Astrophysics, University of Nevada, Las Vegas, NV 89154, USA*

ABSTRACT

We present near-infrared spectroscopy of ten weak emission-line quasars (WLQs) at redshifts of $z \sim 2$, obtained with the Palomar 200-inch Hale Telescope. WLQs are an exceptional population of type 1 quasars that exhibit weak or no broad emission lines in the ultraviolet (e.g., the C IV $\lambda 1549$ line), and they display remarkable X-ray properties. We derive $H\beta$ -based single-epoch virial black-hole masses (median value $1.7 \times 10^9 M_{\odot}$) and Eddington ratios (median value 0.5) for our sources. We confirm the previous finding that WLQ $H\beta$ lines, as a major low-ionization line, are not significantly weak compared to typical quasars. The most prominent feature of the WLQ optical spectra is the universally weak/absent [O III] $\lambda 5007$ emission. They also display stronger optical Fe II emission than typical quasars. Our results favor the super-Eddington accretion scenario for WLQs, where the weak lines are a result of a soft ionizing continuum; the geometrically thick inner accretion disk and/or its associated outflow is responsible for obscuring the nuclear high-energy radiation and producing the soft ionizing continuum. We also report candidate extreme [O III] outflows (blueshifts of ≈ 500 and 4900 km s^{-1}) in one object.

Keywords: accretion, accretion disks – galaxies: active – quasars: emission lines

1. INTRODUCTION

The spectra of type 1 quasars are characterized by strong and broad emission lines in the optical and ultraviolet (UV). These lines are considered to be produced by high-velocity photoionized gas in the broad emission-line region (BELR) that is within the gravitational potential well of the central supermassive black hole (SMBH). The size of the BELR, derived either from reverberation-mapping campaigns or an empirical luminosity–radius relation (e.g., Maoz et al. 1991; Peterson et al. 1991; Kaspi et al. 2000; Bentz et al. 2009; Du et al. 2014), combined with the virial velocity of the BELR obtained from emission-line profiles, provide an effective approach to estimate the masses of SMBHs in distant quasars (e.g., Shen & Liu 2012, and references therein).

A small population (a few hundred) of type 1 quasars have been discovered to exhibit exceptionally weak or no broad emission lines in the UV (e.g., Ly α + N v $\lambda 1240$ complex, C IV $\lambda 1549$, Mg II $\lambda 2799$;

Fan et al. 1999; Diamond-Stanic et al. 2009; Plotkin et al. 2010; Shemmer et al. 2010). These weak emission-line quasars (WLQs) have generally been found at high redshifts ($z \gtrsim 1.5$), where optical spectroscopy covers the rest-frame UV spectrum. There is no uniform emission-line strength definition for WLQs. Typically they are selected to have rest-frame equivalent widths (REWs) $\approx 3\text{--}4\sigma$ below the mean of the REW distribution for the considered UV line. For example, $\text{REW}(\text{Ly}\alpha + \text{N v}) < 15.4 \text{ \AA}$ and $\text{REW}(\text{Ly}\alpha + \text{N v}) < 10 \text{ \AA}$ were adopted in Diamond-Stanic et al. (2009) and Shemmer et al. (2009), respectively, and the lower 3σ limit of the log-normal C IV REW distribution is $\approx 10 \text{ \AA}$ (e.g., Diamond-Stanic et al. 2009; Wu et al. 2012). It also appears difficult to unify WLQ populations identified with different lines (e.g., Wu et al. 2012; Paul et al. 2022). The fraction of WLQs likely increases with redshift. Based on a sample of ~ 3000 Sloan Digital Sky Survey (SDSS; York et al. 2000) quasars in the redshift range of $\sim 3\text{--}5$, Diamond-Stanic et al. (2009) found

that the WLQ fraction is 1.3% (36/2737) below $z \sim 4.2$, and it is 6.2% (20/321) at $z \gtrsim 4.2$. Of 117 Pan-STARRS1 quasars at $5.6 \lesssim z \lesssim 6.7$, Bañados et al. (2016) identified 16 (13.7%) WLQs. Several of the ultraluminous quasars at $z > 4.5$ are also WLQs (e.g., Wu et al. 2015; Wolf et al. 2020). Besides the exceptional emission-line properties, WLQs have typical quasar continuum spectral energy distributions (SEDs) from the infrared (IR) to UV (e.g., Diamond-Stanic et al. 2009; Shemmer et al. 2010; Lane et al. 2011; Wu et al. 2011, 2012; Luo et al. 2015; Plotkin et al. 2015).

The physical mechanism responsible for the remarkable emission-line properties of WLQs is not clear. The weak line emission is not caused by contamination from jet emission, line obscuration, gravitational lensing effects, or broad absorption line (BAL) effects. One possible explanation is that the WLQ BELR is gas deficient due to low gas content and/or a small covering factor (the anemic BELR scenario; e.g., Shemmer et al. 2010). Another possible explanation is that the weak line emission is caused by a “soft” nuclear ionizing continuum that cannot ionize the BELR to the typical ionization state. In the former scenario, one might expect that all broad emission lines of WLQs would be weak. However, simultaneous rest-frame optical and UV spectroscopy of a small sample of six WLQs with VLT/X-Shooter revealed that only the UV C IV lines are substantially weaker (at $> 3\sigma$ levels) than those of typical quasars, while the optical lines such as $H\beta$ $\lambda 4861$ are not significantly weak compared to typical quasars (Plotkin et al. 2015). This result favors the soft ionizing continuum scenario where only the high-ionization BELR is strongly affected, leading to the exceptionally weak C IV emission. Rest-frame optical spectroscopy of a large sample of WLQs is needed to investigate systematically the strength of their $H\beta$ lines and assess whether the soft ionizing continuum scenario is the most probable explanation for WLQs.

Despite the typical IR–UV continuum SEDs of WLQs, they show remarkable X-ray properties. Systematic investigations of the X-ray emission from WLQs have revealed that a significant fraction ($\approx 30 - 50\%$) of them are also distinctly X-ray weak compared to typical quasars (Wu et al. 2011, 2012; Luo et al. 2015; Ni et al. 2018, 2022; Pu et al. 2020). The level of X-ray weakness is often assessed by the deviation from the empirical $\alpha_{\text{OX}}-L_{2500 \text{ \AA}}$ relation (e.g., Steffen et al. 2006),¹ which describes a negative correlation between the relative X-ray emission strength and the optical/UV luminosity. The average X-ray weakness factor for the X-ray weak WLQs is ≈ 13 , and their stacked effective power-law photon index (Γ_{eff}) is flatter ($1.1^{+0.2}_{-0.1}$) than that of

the X-ray normal WLQs (1.8 ± 0.1), suggestive of X-ray obscuration (e.g., Luo et al. 2015; Ni et al. 2022). A few WLQs have been observed to vary between X-ray weak and X-ray nominal-strength states (e.g., Miniutti et al. 2012; Ni et al. 2020, 2022; Liu et al. 2022), and the sometimes rapid variability even suggested an origin of a few tens of gravitational radii (Liu et al. 2022).

Based on the X-ray results and the soft ionizing continuum scenario, it has been proposed that WLQs probably have super-Eddington accretion rates, and a geometrically Thick inner accretion Disk and/or its associated Outflow (TDO) is responsible for obscuring the nuclear high-energy radiation and producing a soft ionizing continuum (e.g., Luo et al. 2015; Ni et al. 2018, 2022; see the schematic diagram in Figure 1 of Ni et al. 2018). In this scenario, the quasar emits nominal levels of IR-to-X-ray radiation (i.e., typical quasar continuum SED) from the torus, accretion disk, and corona. However, the TDO shields the equatorial high-ionization BELR, and thus the ionizing continuum received by the BELR is soft, causing the weak emission lines such as the C IV line. Moreover, if the inclination angle of the quasar is large (i.e., a more edge-on view), and our line of sight intercepts the TDO, we would observe an X-ray obscured (X-ray weak) quasar. The obscuring TDO is probably clumpy, resulting in the (sometimes rapid) X-ray variability observed in a few WLQs. The IR–UV continuum SED is not greatly affected in this scenario. This TDO model can explain, in a simple and unified manner, the weak emission lines, remarkable X-ray properties, and other multiwavelength properties of WLQs. However, it is generally difficult to obtain reliable Eddington-ratio estimates for quasars. The situation becomes worse for high-redshift quasars with only UV spectra, as the C IV-based virial SMBH masses are likely biased or even incorrect (e.g., Baskin & Laor 2005; Denney 2012; Kratzer & Richards 2015; Coatman et al. 2017; Dix et al. 2023). Some of the “Eigenvector 1” parameters have been suggested to be correlated with the accretion rate (e.g., Boroson & Green 1992; Sulentic et al. 2000; Shen & Ho 2014), but measurements of these also require rest-frame optical spectroscopy.

In this study, we present near-IR (NIR) spectra of a sample of ten WLQs observed with the Palomar Hale 200-inch telescope (P200), expanding the currently limited samples of WLQs with rest-frame optical spectra (e.g., Shemmer et al. 2010; Wu et al. 2011; Plotkin et al. 2015; Shemmer & Lieber 2015; Ha et al. 2023). We examine the optical emission-line properties of these WLQs and evaluate the TDO scenario. The paper is organized as follows. We describe the sample selection, P200 data reduction, spectral analysis, and high- z comparison samples in Section 2. In Section 3, we present the emission-line properties and relevant comparisons; we also provide SMBH mass and Eddington-ratio estimates. We

¹ α_{OX} is defined as $\alpha_{\text{OX}} = -0.3838 \log(f_{2500 \text{ \AA}}/f_{2 \text{ keV}})$, with $f_{2500 \text{ \AA}}$ and $f_{2 \text{ keV}}$ being the rest-frame 2500 Å and 2 keV flux densities, respectively. $L_{2500 \text{ \AA}}$ is the 2500 Å monochromatic luminosity.

discuss our results in the context of the TDO scenario in Section 4, and we report candidate extreme [O III] $\lambda 5007$ outflows in one of the sources. We summarize our main results in Section 5. In the Appendix, we present the spectrum of a low- z WLQ candidate that had an incorrect redshift in the SDSS quasar catalog. Throughout this paper, we use a cosmology with $H_0 = 67.4 \text{ km s}^{-1} \text{ Mpc}^{-1}$, $\Omega_M = 0.315$, $\Omega_\Lambda = 0.685$ (Planck Collaboration et al. 2020). Uncertainties are quoted at a 1σ confidence level, and upper limits are at a 3σ confidence level.

2. SAMPLE SELECTION AND NEAR-INFRARED SPECTROSCOPY

2.1. Sample Selection and P200/TSpec Observations

We first selected our WLQ targets from the SDSS Data Release 7 (DR7; Abazajian et al. 2009) quasar catalog (Shen et al. 2011). We chose radio-quiet quasars ($R_{6\text{cm}_2500\text{\AA}} < 10$ in the Shen et al. 2011 catalog) in the redshift range of $1.7 < z < 2.2$. Radio-quiet quasars were chosen to avoid possible amplified (beamed) continua associated with relativistic jets, and the redshift range was chosen to have good coverage of the C IV and Mg II line profiles in the SDSS spectra. We excluded BAL quasars by requiring $\text{BAL_FLAG} = 0$ in the Shen et al. (2011) DR7 quasar catalog. BAL quasars may have biased [C IV] REW measurements due to the line absorption; they are also generally X-ray absorbed (e.g., Gallagher et al. 2002, 2006). For economical observations, we selected bright (i -band magnitude $m_i \leq 18.2$) quasars. We required the C IV emission-line signal-to-noise ratio ($\text{SNR} > 5$ ($\text{LINE_MED_SN_CIV}] > 5$ in the Shen et al. 2011 catalog). Early studies employed the conservative $\text{REW} < 5 - 10 \text{ \AA}$ criterion to select C IV WLQs (e.g., Plotkin et al. 2010; Wu et al. 2012; Luo et al. 2015). However, Ni et al. (2018, 2022) constructed a representative sample of WLQs using a more inclusive criterion of $\text{REW} < 15 \text{ \AA}$, which still show consistent multi-wavelength properties. Therefore, we adopted a threshold of $\text{C IV REW} < 15 \text{ \AA}$ for the initial selection. We further supplemented our sample with the WLQs (29 unique WLQs after excluding objects in common) from Luo et al. (2015) that have C IV measurements and X-ray observations. They have different redshift ($1.65 < z < 2.92$) and i -band magnitude ($15.4 \leq m_i \leq 18.5$) ranges from the SDSS DR7 selected targets. Our observations were carried out with the Triple Spectrograph (TSpec) mounted on P200, which has spectral coverage of $\approx 0.95\text{--}2.46 \mu\text{m}$ and spectral resolutions of $\approx 2500\text{--}2700$ (Herter et al. 2008). We enforced an additional redshift filtering: $z < 1.67$ and $2.08 < z < 2.65$, so that the broad $\text{H}\beta$ emission line will not be significantly affected by telluric absorption. We also excluded two objects with existing NIR spectra from Wu et al. (2011) or Plotkin et al.

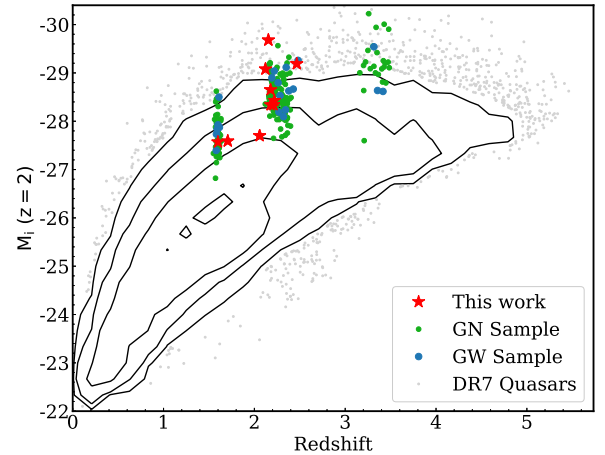


Figure 1. Absolute i -band magnitude vs. redshift for our ten objects (red stars). The underlying gray dots and black contours represent the distribution of objects in the SDSS DR7 quasar catalog. The lowest contour level denotes $10^{1.6}$ quasars per bin (25 bins along each axis), and the increasing contours are logarithmically spaced by 0.6 dex; individual gray points are quasars falling below the lowest contour level. Our sources are among the most luminous quasars. The green and blue dots represent the GW and GN samples from the Matthews et al. (2023) GNIRS-DQS catalog that constitute our comparison samples.

(2015). The parent sample constructed this way contains 28 WLQs.

We obtained 1.5 nights of good P200/TSpec observations in 2021 April and May via China’s Telescope Access Program (TAP).² We used a $1'' \times 30''$ slit with standard ABBA nodding along the slit. The exposure time for each target was either 40 or 60 minutes. For flux calibration and telluric correction, we observed an A0V standard star before or after each observation. The star was chosen so that the observation airmasses for the WLQ target and the star are comparable. We obtained high SNR ($\gtrsim 10$) NIR spectra for 11 objects in the parent sample, which are all in the Shen et al. (2011) SDSS DR7 quasar catalog. The basic information of these observations is presented in Table 1. One target, SDSS J164302.03+441422.1, turned out to have an incorrect redshift in the Shen et al. (2011) DR7 quasar catalog, and thus the WLQ identification was not reliable. We removed this object from our sample; the spectrum of SDSS J164302.03+441422.1 is presented in the Appendix. The remaining ten objects constitute the final sample of this study. Among these ten sources, nine have C IV REW $< 10 \text{ \AA}$ and four have X-ray coverage from Wu et al. (2012), Luo et al. (2015), or Ni et al. (2022).

² <https://tap.china-vo.org/>.

2.2. Data Reduction

We reduced raw P200/TSpec observational data following the standard procedure, described briefly below. The modified IDL-based Spextool 4 package (Cushing et al. 2014) was used for data reduction. We first constructed dark and flat-field files. For each source, wavelength calibration was then performed based on automatic identification of telluric airglow lines in the spectra of the corresponding standard star. We extracted one-dimensional spectra with the “A–B” method to subtract background. Each source thus has 8 (for 40-minute exposures) or 12 (for 60-minute exposures) spectra and each spectrum consists of four orders that are to be merged in the end. We combined the spectra for each object by scaling them to the spectrum that has the highest flux level in the $H\beta$ region (rest-frame 4360–5360 Å) and then stacking all the spectra. The brightest spectrum is likely the least affected by guiding errors and variable sky transmission, and thus it is considered the most accurate spectrum for flux normalization.

We then corrected telluric absorption following the procedure described in Vacca et al. (2003). We first extracted spectra of the corresponding standard star with the same approach above. Given the B - and V -band magnitudes of the star, we created a model spectrum of Vega, convolved to the spectral resolution of the combined star spectra. The model spectrum was then divided by the star spectrum to yield a telluric correction spectrum. We visually inspected each telluric correction spectrum and verified that there are no significant residual hydrogen lines. We multiplied the object spectrum by the telluric correction spectrum to produce a flux-calibrated and telluric-corrected spectrum. Finally, we merged the four orders in each spectrum by normalizing them using the overlapping regions; typically the scaling factors are close to unity (≈ 0.97 – 1.05) between the orders.

We examined the quality of the final spectra. The average SNRs per pixel in the $H\beta$ region for our ten sources range from ≈ 10 to ≈ 50 (with a median value of ≈ 17), sufficient for basic spectral analysis. We also compared our spectra to the available SDSS spectra by dividing them in the overlapping regions. The average ratios range from 0.75 to 1.42 with a median value of 0.95. These flux uncertainties are likely dominated by systematic uncertainties in the above flux calibration procedure, with additional contributions from the SDSS flux calibration uncertainties and quasar flux variability over timescales of years (e.g., Shen 2021; Suberlak et al. 2021).

2.3. Spectral Analysis

Spectral analyses of the P200/TSpec spectra were performed with the PyQSOFit package (v1.1),³ which uses a χ^2 -based method to fit the continuum and emission lines (e.g., Shen et al. 2011; Guo et al. 2018, 2019). PyQSOFit first applied Galactic extinction corrections to the spectra using the $E(B-V)$ values from Schlegel et al. (1998) and the Galactic extinction curve from Fitzpatrick (1999) with $R_V = 3.1$. Our continuum model consists of a power-law component, a polynomial component, the Boroson & Green (1992) optical Fe II emission template, and a Balmer-continuum template. The Balmer-continuum component is not needed for six of the ten sources. The polynomial component is used to account for spectral complexity such as reddening, and it is not needed for four sources. The fitting was performed using line-free windows around major broad emission lines (e.g., 6000–6250 Å and 6800–7000 Å around $H\alpha$, 4435–4630 Å and 5100–5535 Å around $H\beta$). Given the best-fit continuum, we derived the monochromatic luminosity at 5100 Å (L_{5100}) from the power-law component + the polynomial component (if present), and we measured the REW of the Fe II pseudo continuum between 4434 and 4684 Å against the underlying continuum.

After subtracting the best-fit continuum, we fitted the emission lines with multiple Gaussian profiles. All line fits were performed in the rest frame. For AGN broad emission-lines, a single Gaussian function usually cannot explain the line profile, and multiple Gaussian profiles (sometimes with additional Lorentzian profiles) are often employed to fit the lines (e.g., Shen et al. 2011; Perna et al. 2015; Plotkin et al. 2015; Du & Wang 2019; Guo et al. 2019). The reason behind this is complex. It might be due to a combination of line asymmetries from absorption or outflows, broad-line stratification, and inaccurate subtraction of the continuum (including the Fe II pseudo continuum). Because of these effects, the multiple Gaussian profiles used to fit the lines do not carry individual physical significance. For example, the velocity offsets of individual components usually do not represent outflow velocities. The line parameters (e.g., REW, FWHM, flux) are thus typically measured using the combined line profile.

For the $H\beta$ line, we used up to three Gaussians, including two broad components with full widths at half maximum (FWHMs) ≥ 1200 km s⁻¹ and one narrow component with FWHM < 1200 km s⁻¹; this 1200 km s⁻¹ line-width criterion also applies to other lines in this study. Among the ten sources, seven require two broad components and the other three have only one broad component. Only one source shows a clear narrow $H\beta$ component. Following Shen et al. (2011), we adopted a Monte-Carlo approach to obtain uncertainties of the best-fit parameters. For each source, 1000

³ <https://github.com/legolason/PyQSOFit>.

Table 1. P200/TSpec Observation Log

Source Name (SDSS J)	z_{dr7}^a	z_{p200}	i_{psf}^b (mag)	M_i^c (mag)	Obs. Date	Exp. Time (min)	Ref _X ^d
073306.63+462517.5	2.133	2.179	17.43	-28.65	2021-04-02	40	-
085344.17+354104.5	2.175	2.179	17.72	-28.34	2021-04-02	40	-
111401.30+222211.4	2.121	2.058	18.20	-27.70	2021-04-02	40	-
122709.48+310749.3	2.171	2.220	17.58	-28.43	2021-04-02	40	-
134601.28+585820.2	1.646	1.707	17.58	-27.59	2021-05-21	60	(2), (3)
153412.68+503405.3	2.118	2.122	16.83	-29.08	2021-04-02	40	(2)
153714.26+271611.6	2.458	2.467	17.20	-29.19	2021-04-02	40	(2)
154329.47+335908.7	2.148	2.154	16.28	-29.68	2021-05-21	60	-
154503.23+015614.7	2.195	2.211	17.83	-28.34	2021-05-21	60	-
161245.68+511816.9	1.595	1.599	17.55	-27.57	2021-05-21	60	(1)
164302.03+441422.1*	1.650	0.919	18.39	-26.81	2021-05-21	60	(2)

^aRedshift from Shen et al. (2011).

^bSDSS *i*-band point-spread function (PSF) magnitude from Schneider et al. (2010).

^cAbsolute *i*-band magnitude (*K*-corrected to $z = 2$) from Shen et al. (2011).

^dReference papers for the objects with published X-ray data. (1): Wu et al. (2012); (2): Luo et al. (2015); (3): Ni et al. (2022).

*This object has an incorrect redshift in the Shen et al. (2011) catalog. It is a WLQ candidate and it is not included in our final sample.

mock spectra were created by randomizing the spectrum with the Gaussian noise at individual pixels. We then fitted the mock spectra following the same procedure above, and the 1σ dispersion of the 1000 measurements for each parameter was adopted as its uncertainty.

We used two narrow Gaussians and two broad Gaussians to fit the [O III] $\lambda 4959, 5007$ doublet; we fixed the flux ratio of the narrow components to the theoretical value of 3.0 (i.e., $f_{5007}/f_{4959} = 3$). We tied the velocity offsets of the narrow H β line and the [O III] $\lambda 4959, 5007$ doublet if they are available. Some sources do not show clear [O III] lines. We consider the [O III] $\lambda 5007$ line to be detected if the best-fit REW exceeds three times the 1σ dispersion determined from the Monte Carlo approach above. Four sources have narrow [O III] $\lambda 5007$ REW measurements and another object, SDSS J153714.26 + 271611.6, appears to have broad [O III] components. The broad components have significant blueshifts and might indicate large-scale ionized outflows in this quasar (see Section 4.2 below), and thus we do not consider the broad components part of typical AGN [O III] emission. For the six objects without narrow [O III] lines, we present their 3σ upper limits on the [O III] $\lambda 5007$ REWs; such stringent upper limits were adopted mainly for the survival analysis in Section 3.1 below.

For the H α complex, we adopted up to three broad Gaussians and one narrow Gaussian for the H α line, and we used up to four narrow Gaussians to model the [N II] and [S II] lines. We enforced a fixed flux ratio for the narrow [N II] lines by setting $f_{6584}/f_{6548} = 3$ (e.g., Shen et al. 2011), as the lines are typically located on top of the broad H α profile core. We tied the velocity offsets of the narrow H α line and the [N II] and [S II] line sets. However, we did not tie these velocity offsets to those of the narrow H β and [O III] lines as the latter lines are often weak or absent. Basic emission-line parameters, including REW, FWHM, and line flux, were derived from the combined broad or narrow components for each line.

We improved the redshifts of our sources using the P200/TSpec spectra. Their redshifts from the SDSS DR7 quasar catalog (Shen et al. 2011) are listed in Table 1, which are consistent with those in Hewett & Wild (2010). These redshifts were derived based on mainly the weak and sometimes blueshifted UV emission lines (e.g., C IV and Mg II). Since the majority of our sources do not show clear [O III] line emission in the P200/TSpec spectra, we obtained their redshifts from the peak positions of the broad H α and H β emission-line profiles adopting an iterative procedure. The Shen et al. (2011) redshift was used as the initial input in PyQSOFit. We then measured a new redshift from the av-

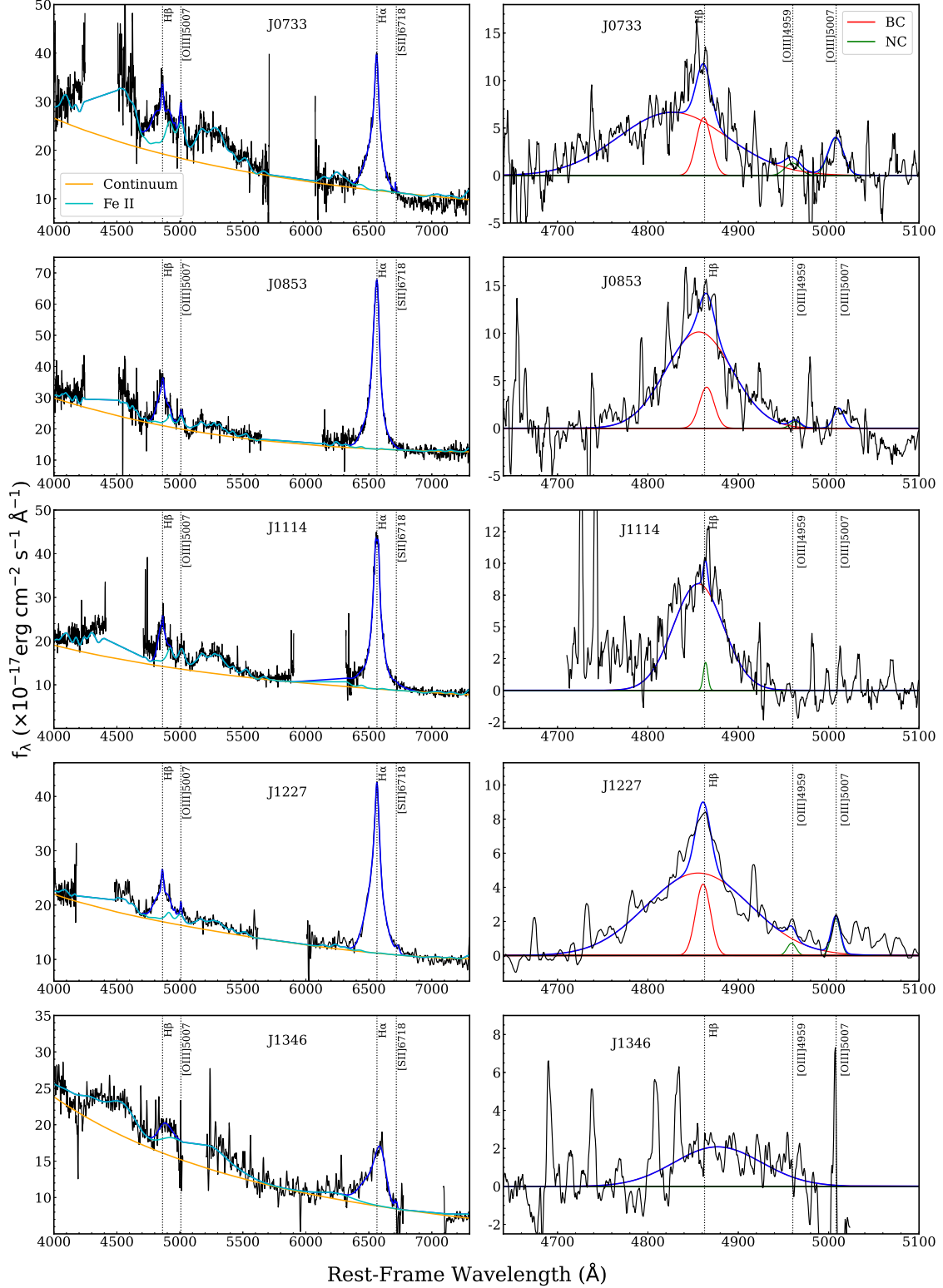


Figure 2. Rest-Frame optical spectra for our ten sources and the best-fit models. Positions of major emission lines are marked. The left panel shows the broad-band spectra (black curves) smoothed with box convolutions (ranging from 5 to 10 pixels). The blue curve represents the best-fit continuum + emission-line model, The orange curve shows the power-law + polynomial (if present) continuum, and the cyan curve shows the Fe II pseudo continuum. The right panel shows zoomed-in views of the spectra in the $H\beta$ region, fitted with broad (red curves) and/or narrow (green curves) Gaussian profiles for the $H\beta$ and [O III] emission lines.

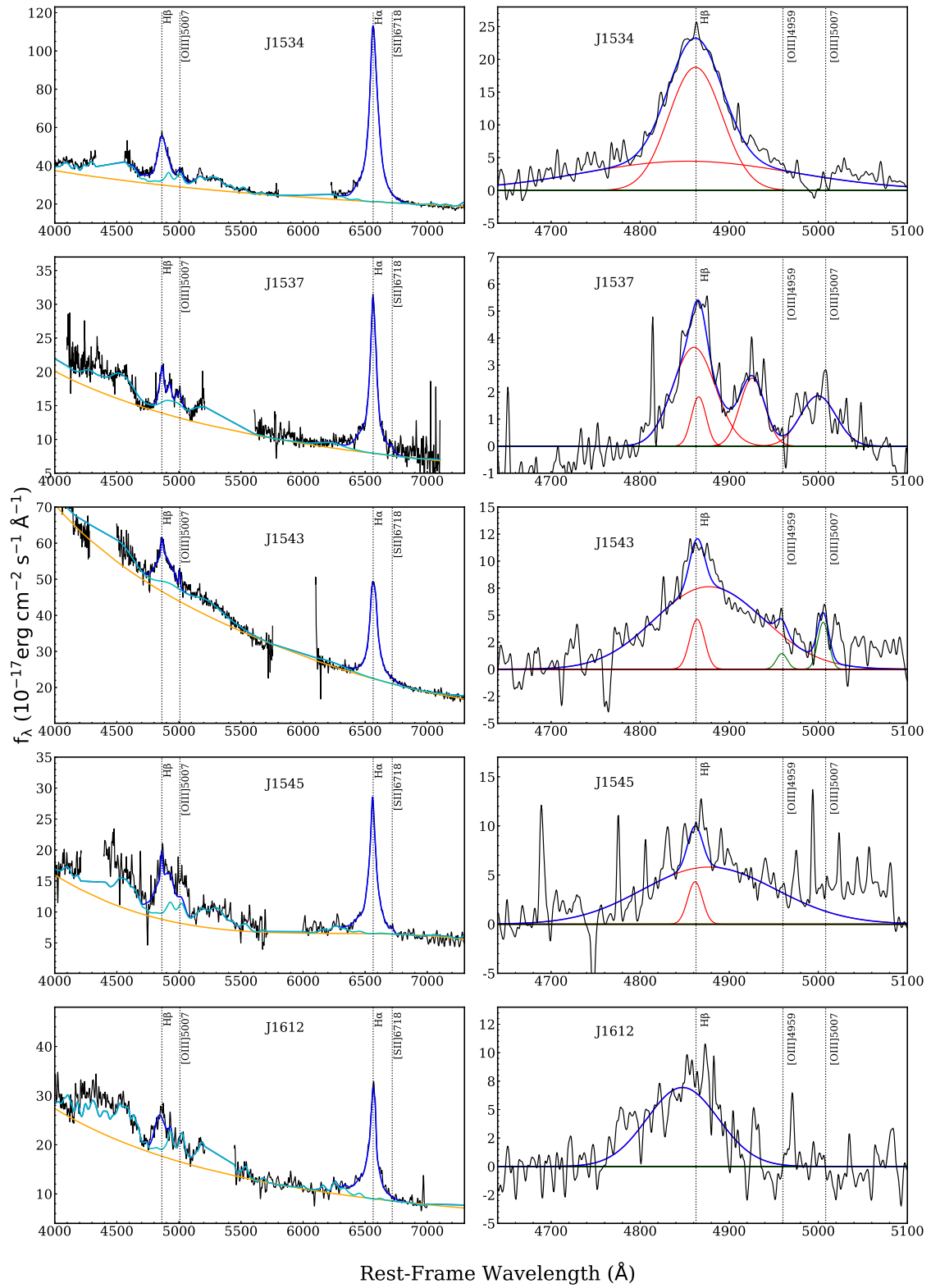


Figure 2 (Cont.).

erage velocity offset of the best-fit $H\alpha$ and $H\beta$ broad components. The new redshift was used in the next iteration. If the redshift difference is smaller than 0.001, we considered the value converged and stopped the iteration. The resulting redshifts are listed in Table 1, and they differ slightly (in the range of -0.063 – 0.061 with an average value of -0.014) from the Shen et al. (2011) redshifts for our ten sources. We adopt the P200/TSpec redshifts in the following analyses.

We show the absolute i -band magnitude versus redshift distribution for our sources in Figure 1; these are luminous quasars compared to typical SDSS DR7 quasars due to our selection of bright targets. The spectra and the best-fit models are displayed in Figure 2, and the emission-line measurements are summarized in Table 2.

2.4. High- z Comparison Samples

To identify distinct features in the NIR spectra of the WLQs in our sample, we selected comparison samples that consist of high-redshift quasars with NIR spectra. These were drawn from the 260 quasars in the Gemini Near Infrared Spectrograph-Distant Quasar Survey (GNIRS-DQS; Matthews et al. 2021, 2023), which is a homogeneous flux-limited NIR spectroscopic survey of high-redshift quasars. We first chose the 199 GNIRS-DQS quasars that are also in the Shen et al. (2011) SDSS DR 7 quasar catalog in order to have good C IV REW measurements ($\text{LINE_MED_SN_CIV}] > 5$) from that catalog, consistent with our target selection. We then excluded significantly radio-loud ($R > 100$)⁴ quasars from this sample as the optical continua of these quasars might have potential contamination from non-thermal jet radiation. To obtain the radio-loudness parameters, we matched the GNIRS-DQS objects to the catalogs of the Faint Images of the Radio Sky at Twenty-cm (FIRST; Becker et al. 1995) survey and the NRAO Very Large Array (VLA) Sky Survey (NVSS; Condon et al. 1998) with matching radii of $5''$ and $30''$, respectively. A radio power-law spectral slope of $\alpha_r = -0.8$ was adopted to convert 1.4 GHz flux densities to 5 GHz flux densities. Nine GNIRS-DQS quasars, all detected in FIRST, have $R > 100$ and they were excluded from the comparison samples, leaving 190 GNIRS-DQS quasars.

There are also WLQs in the GNIRS-DQS sample. Adopting the same C IV REW $< 15 \text{ \AA}$ criterion using the SDSS DR7 measurements, we identified 22 WLQs (12 having REW $< 10 \text{ \AA}$), two of which are in common with our objects (SDSS J085344.17+354104.5 and SDSS J122709.48+310749.3). After excluding these WLQs, we refer to the remaining 168 (190–22) quasars as the Gemini-normal (GN)

sample which is our comparison sample of typical quasars. For the 20 GNIRS-DQS WLQs (excluding the two objects in common), the measurements were obtained from a different instrument with a different spectral analysis approach. We thus do not consider it appropriate to combine them with our objects to construct a larger sample. Instead, we consider these 20 WLQs the Gemini-weak (GW) sample, and also compare our sample properties to theirs. The absolute i -band magnitude versus redshift distributions for the two comparison samples are also shown in Figure 1. Except for the $z > 3$ objects, they occupy similar regions as the WLQs in our sample. We have verified that excluding the 24 (3) $z > 3$ quasars from the GN (GW) sample does not change our comparison results in Section 3.1 below.

Measurements of the $H\beta$, [O III], and Fe II emission lines for the two comparison samples are adopted from Matthews et al. (2023). As a consistency check, we randomly selected ten quasars in the comparison samples and measured their emission-line properties using the GNIRS-DQS spectra, and the results are overall consistent with those in Matthews et al. (2023). For the two WLQs in common, SDSS J085344.17+354104.5 and SDSS J122709.48+310749.3, we also compared their P200 and GNIRS-DQS measurements. The emission-line properties for SDSS J085344.17+354104.5 are consistent within the errors, but they differ by up to $\approx 50\%$ for SDSS J122709.48+310749.3, which are likely attributed to systematic uncertainties from the flux calibration and spectral analysis approaches. We do not observe any systematic bias between our data analysis procedure and that in Matthews et al. (2023), and thus statistical comparisons of the sample properties should guard against such uncertainties. Matthews et al. (2023) have a different [O III] detection threshold for the GNIRS-DQS quasars and objects with [O III] REWs below 1 \AA were considered non-detections. We set their REW upper limits to 5 \AA following Matthews et al. (2021). As objects with [O III] non-detections constitute a small fraction (10%) in the GN sample and a large fraction (45%) in the GW sample, the exact upper-limit value for the non-detections does not change qualitatively our statistical comparison results in Section 3.1 below.

3. RESULTS

3.1. Emission-Line Properties and Comparisons

The main aim of this study is to examine the rest-frame optical spectroscopic properties of WLQs. The best-fit continuum shapes of our objects, determined from the power-law component + the polynomial component (if present; Section 2.3), appear to be similar to those of typical SDSS quasars (e.g., Vanden Berk et al. 2001). Nominal optical continuum shapes were also reported for the WLQ sample in Plotkin et al. (2015). These are consistent with the typical

⁴The radio-loudness parameter (R) is defined as $R = f_{5 \text{ GHz}}/f_{4400 \text{ \AA}}$ (Kellermann et al. 1989), where $f_{5 \text{ GHz}}$ and $f_{4400 \text{ \AA}}$ are the flux densities at 5 GHz and 4400 \AA , respectively.

Table 2. Emission-Line Properties

Source Name (SDSS J)	H β REW (\AA)	[O III] λ 5007 REW ^a (\AA)	Fe II REW (\AA)	H β FWHM (km s^{-1})	Fe II FWHM (km s^{-1})	C IV REW ^c (\AA)
073306.63+462517.5	58.8 ± 1.4	4.5 ± 0.6	101 ± 36	4900 ± 280	3290 ± 2100	6.4 ± 1.2
085344.17+354104.5	50.7 ± 0.7	1.7 ± 0.4	36 ± 2	3780 ± 210	1740 ± 80	3.5 ± 0.8
111401.30+222211.4	55.4 ± 1.4	< 0.98	79 ± 9	4450 ± 310	2410 ± 140	3.9 ± 0.9
122709.48+310749.3	45.1 ± 1.4	1.7 ± 0.2	30 ± 4	2700 ± 270	2420 ± 170	13.5 ± 1.1
134601.28+585820.2	17.3 ± 1.3	< 0.91	56 ± 5	6990 ± 1100	10000^b	2.4 ± 0.9
153412.68+503405.3	91.1 ± 1.5	< 3.3	59 ± 3	5040 ± 65	2390 ± 600	9.2 ± 0.9
153714.26+271611.6	24.9 ± 0.4	< 3.1	50 ± 2	2500 ± 1200	4870 ± 250	7.9 ± 0.7
154329.47+335908.7	25.7 ± 0.4	1.5 ± 0.3	25 ± 1	5090 ± 190	10000^b	8.1 ± 0.5
154503.23+015614.7	134.6 ± 4.8	< 13.1	88 ± 11	5130 ± 1400	3150 ± 260	9.6 ± 0.9
161245.68+511816.9	25.4 ± 1.4	< 2.0	70 ± 4	4870 ± 360	2370 ± 360	1.6 ± 1.9

^aMeasurement or upper limit for the narrow [O III] λ 5007 REW. SDSS J153714.26 + 271611.6 appears to have broad [O III] components (see Section 4.2 below).

^bThis FWHM value pegged at 10000 km s^{-1} , the upper bound allowed by our PyQSOFit fitting.

^cThe C IV REW is adopted from Shen et al. (2011).

quasar IR–UV continuum SEDs observed for WLQs (e.g., Lane et al. 2011; Luo et al. 2015; Ni et al. 2018). Therefore, we focus below on the investigation of emission-line properties.

The emission-line features we examined include the [O III] λ 5007 REW ($W_r[\text{O III}]$), H β REW ($W_r[\text{H}\beta]$), H β FWHM (FWHM[H β]), optical Fe II REW ($W_r[\text{Fe II}]$), and $R_{\text{Fe II}}$ ($W_r[\text{Fe II}]/W_r[\text{H}\beta]$). For statistical comparisons to the comparison samples, we ran the Peto-Peto Generalized Wilcoxon (P-P) test in the Astronomy Survival Analysis package (ASURV; e.g., Feigelson & Nelson 1985; Lavalley et al. 1992) for the $W_r[\text{O III}]$ measurements which contain censored data, and we ran the Kolmogorov-Smirnov (K-S) test for the other quantities. The test results (test statistics and null-hypothesis probabilities) are listed in Table 3. The distributions of $W_r[\text{O III}]$, $W_r[\text{H}\beta]$, FWHM[H β] and $R_{\text{Fe II}}$ for our sample and the comparison samples are displayed in Figure 3.

With only four objects having measurable [O III] emission lines (Table 2), the WLQs in our sample show noticeably weak [O III] emission compared to the GN sample ($P_{\text{null}} = 3 \times 10^{-6}$). There appears to be a small difference between the $W_r[\text{O III}]$ distributions of our sample and the GW sample ($P_{\text{null}} = 0.007$). We ran a ASURV P-P test on the GW versus GN sample, and they show significantly different $W_r[\text{O III}]$ distributions ($P_{\text{null}} = 2 \times 10^{-6}$). Thus, the GW quasars still show weaker [O III] emission than typical quasars. As one of the Eigenvector 1 parameters, $W_r[\text{O III}]$

Table 3. Statistical Test Results for the Emission-Line Properties of Our Sample and the Comparison Samples

Parameter	Test samples	Peto-Peto Generalized Wilcoxon or Kolmogorov-Smirnov Test ^a	
		Statistic	P_{null}
$W_r[\text{O III}]$	P200 vs. GN	4.70	3×10^{-6}
	P200 vs. GW	2.69	0.007
$W_r[\text{H}\beta]$	P200 vs. GN	0.41	0.06
	P200 vs. GW	0.30	0.57
FWHM[H β]	P200 vs. GN	0.24	0.58
	P200 vs. GW	0.40	0.22
$W_r[\text{Fe II}]$	P200 vs. GN	0.59	0.001
	P200 vs. GW	0.50	0.06
$R_{\text{Fe II}}$	P200 vs. GN	0.71	3×10^{-5}
	P200 vs. GW	0.35	0.37

^aThe Peto-Peto Generalized Wilcoxon test was run for the $W_r[\text{O III}]$ comparison, and the Kolmogorov-Smirnov tests were run for the other comparisons.

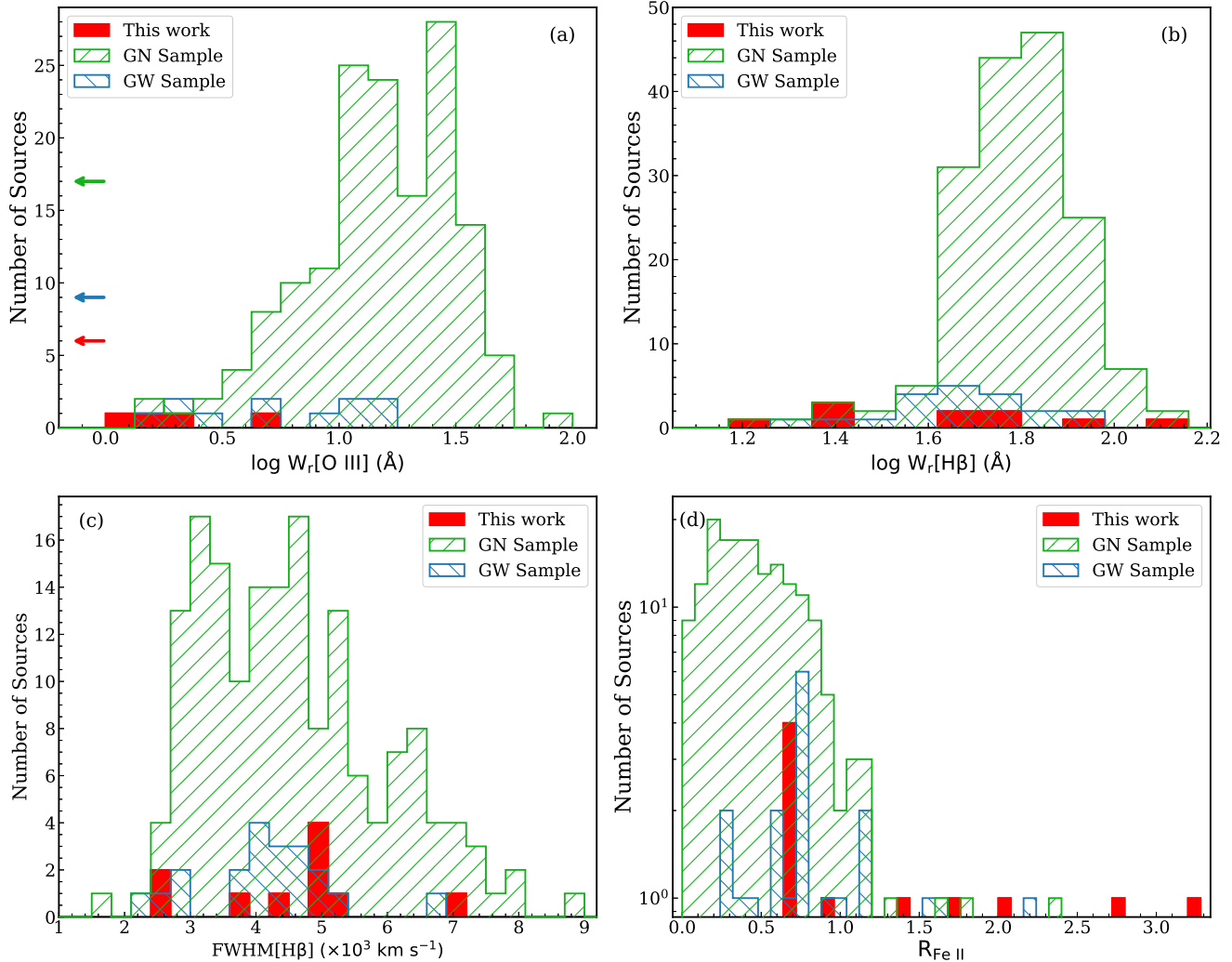


Figure 3. Distributions of (a) $\log W_r[\text{O III}]$, (b) $\log W_r[\text{H}\beta]$, (c) $\text{H}\beta$ FWHMs, and (d) $R_{\text{Fe II}}$ for our WLQ sample. For comparison, the distributions for the GW and GN samples are also shown in each panel. For the $W_r[\text{O III}]$ distributions, upper limits are indicated by the leftward arrows and the y-axis values of the arrows represent the numbers of sources with upper limits in the corresponding samples. Our WLQs show weak $W_r[\text{O III}]$ and stronger Fe II emission compared to typical quasars. Their $\text{H}\beta$ emission is not particularly weak (K-S test $P_{\text{null}} = 0.06$).

has been suggested to be negatively correlated with the accretion rate (e.g., Boroson & Green 1992; Sulentic et al. 2000; Shen & Ho 2014). Thus, it is not surprising to observe WLQs with weak [O III] emission under the scenario that these are super-Eddington accreting with soft ionizing continua from TDO obscuration. In the literature, both of the two WLQs in Shemmer et al. (2010) show weak [O III] emission. Only two objects in the WLQ sample of Plotkin et al. (2015) have good [O III] coverage, and they both show weak [O III] emission. In Ha et al. (2023), the two new WLQs with NIR spectroscopy (see their Appendix) do not show any detectable [O III] emission lines. PHL 1811, a well-studied luminous WLQ at $z = 0.192$, lacks [O III] emission in its optical spectrum (e.g., Leighly et al. 2007). J1521+5202, the only

PHL 1811 analog in Wu et al. (2011) with an NIR spectrum, does not show apparent [O III] emission either. A recent James Webb Space Telescope (JWST) Near-Infrared Camera (NIRCam) spectrum of the $z = 6.327$ WLQ, J0100+2802 (Wu et al. 2015), shows no narrow [O III] emission either (Eilers et al. 2023).

Weak [O III] emission has also been observed in other high- z luminous quasar samples. For example, $\approx 70\%$ of the WISE/SDSS selected hyper-luminous (WISSH) quasars show weak or absent [O III] emission; several of these also show weak X-ray emission and a few have $\text{C IV REW} < 15 \text{ \AA}$ and could be considered WLQs (e.g., Vietri et al. 2018; Zappacosta et al. 2020).

Our WLQ sample does not show significantly weaker $H\beta$ emission (average $W_r[H\beta] \approx 52.9 \pm 2.0 \text{ \AA}$) compared to the GN sample (average $W_r[H\beta] \approx 64.4 \pm 8.1 \text{ \AA}$). The K-S test also suggests that the two $H\beta$ REW distributions do not differ much ($P_{\text{null}} = 0.06$). The $H\beta$ REW distributions for our sample and the GW sample are similar ($P_{\text{null}} = 0.57$). Plotkin et al. (2015) found that the WLQ $H\beta$ lines are toward the weaker end of the distribution for typical quasars, but they are not as exceptionally weak as for the high-ionization C IV lines. For the $H\beta$ FWHMs, there is no significant difference between our sample and the comparison samples; the average $H\beta$ FWHMs for our WLQ sample is $4540 \pm 710 \text{ km s}^{-1}$. It has been suggested that the FWHMs of the $H\beta$ lines have an orientation dependence (e.g., Wills & Browne 1986; Runnoe et al. 2013; Shen & Ho 2014), and larger FWHMs generally correspond to larger inclination angles. WLQs probably do not have unusual inclination angles compared to typical quasars at similar redshifts, although it may be interesting to compare the $H\beta$ FWHMs between X-ray weak and X-ray normal WLQs (see discussion in Section 4.1 below).

Stronger optical Fe II emission appears to be another distinct feature of WLQs. The probability that the $W_r[\text{Fe II}]$ distributions of our WLQ sample and the GN sample are drawn from the same parent population is only $P_{\text{null}} = 0.001$. The difference is enhanced ($P_{\text{null}} = 3 \times 10^{-5}$) if $R_{\text{Fe II}}$ is considered due to the slightly weaker $H\beta$ emission for WLQs. The $W_r[\text{Fe II}]$ and $R_{\text{Fe II}}$ distributions for our sample and the GW sample are similar ($P_{\text{null}} = 0.06$ and $P_{\text{null}} = 0.37$, respectively). Similar findings have been reported for the WLQs in Shemmer et al. (2010) and Plotkin et al. (2015). Being another important Eigenvector 1 parameter, $R_{\text{Fe II}}$ is negatively correlated with $W_r[\text{O III}]$, and large $R_{\text{Fe II}}$ values are likely also driven by high accretion rates (e.g., Boroson & Green 1992; Sulentic et al. 2000; Shen & Ho 2014), consistent with the super-Eddington scenario for WLQs. Following Shen & Ho (2014), we plot in Figure 4 the $\text{FWHM}[H\beta]$ versus $R_{\text{Fe II}}$ distributions with color-coded $W_r[\text{O III}]$ for our sample and the comparison samples. In general, the WLQs show weaker [O III] emission, enhanced Fe II emission, and typical $H\beta$ FWHM values. A few objects (e.g., SDSS J134601.28+585820.2, the rightmost data point) appear to be outliers in the $\text{FWHM}[H\beta]$ versus $R_{\text{Fe II}}$ correlation for typical quasars (e.g., Boroson & Green 1992; Shen & Ho 2014), but these could be explained with object-to-object intrinsic scatter of the correlation or systematic uncertainties from the spectral analysis.

3.2. SMBH Mass and Eddington-Ratio Estimates

With the rest-frame optical spectra that cover the $H\beta$ lines, we are able to estimate more reliably the single-epoch virial SMBH masses for our sources. We adopted the Bentz et al. (2009) formula:

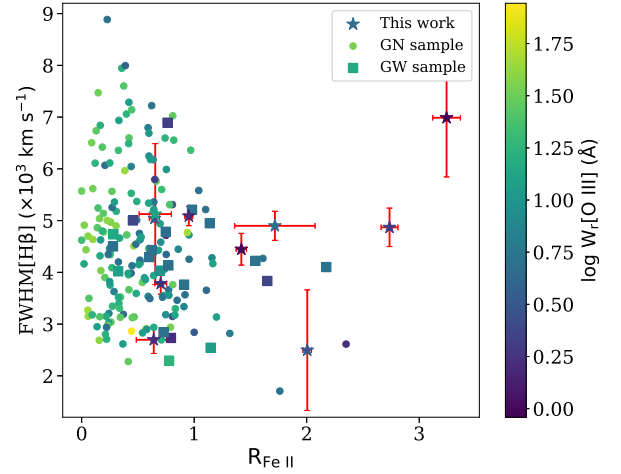


Figure 4. $\text{FWHM}[H\beta]$ vs. $R_{\text{Fe II}}$ for our sample (stars), the GN sample (dots), and the GW sample (squares). We color-code the points by $W_r[\text{O III}]$ to illustrate the distribution of these quasars in the Eigenvector 1 plane. The error bars for the comparison samples are not shown for display purposes. Compared to typical quasars, WLQs show stronger optical Fe II emission and weaker [O III] emission in general.

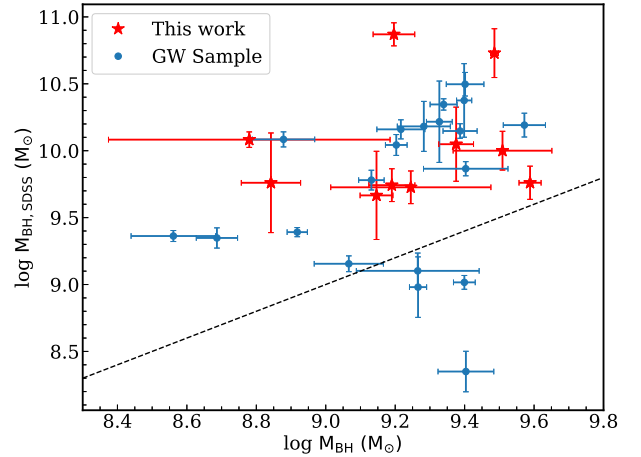


Figure 5. Comparison between the $H\beta$ -based virial SMBH masses derived in this study and Mg II- or C IV-based virial SMBH masses in the SDSS DR7 catalog for our WLQs. The black dashed line is the line of equality. We show also the comparison for the GW sample. The Mg II- or C IV-based virial SMBH masses are systematically larger.

$$\frac{M_{\text{BH}}}{10^6 M_{\odot}} = 5.05 \left[\frac{L_{5100}}{10^{44} \text{ erg s}^{-1}} \right]^{0.5} \left[\frac{\text{FWHM}(H\beta)}{10^3 \text{ km s}^{-1}} \right]^2, \quad (1)$$

Table 4. Virial SMBH Masses and Eddington Ratios

Source Name (SDSS J)	$\log L_{5100}$ (erg s^{-1})	$\log M_{\text{BH}}$ (M_{\odot})	$L_{\text{bol}}/L_{\text{Edd}}$
073306.63+462517.5	46.51	9.38 ± 0.05	0.46 ± 0.06
085344.17+354104.5	46.50	9.15 ± 0.05	0.76 ± 0.08
111401.30+222211.4	46.32	9.20 ± 0.05	0.48 ± 0.07
122709.48+310749.3	46.48	8.84 ± 0.09	1.47 ± 0.29
134601.28+585820.2	46.16	9.51 ± 0.14	0.18 ± 0.06
153412.68+503405.3	46.68	9.49 ± 0.01	0.48 ± 0.01
153714.26+271611.6	46.49	8.78 ± 0.40	1.73 ± 1.62
154329.47+335908.7	46.87	9.59 ± 0.03	0.54 ± 0.04
154503.23+015614.7	46.17	9.24 ± 0.23	0.33 ± 0.17
161245.68+511816.9	46.15	9.19 ± 0.07	0.36 ± 0.05

NOTE—The uncertainties are measurement uncertainties propagated from the uncertainties of the relevant parameters in Equation 1, and they do not include systematic uncertainties associated with the virial mass estimates.

The same formula was used in Plotkin et al. (2015) for their WLQ sample. The resulting SMBH masses are listed in Table 4. Our WLQs are massive SMBHs with $\log(M_{\text{BH}}/M_{\odot})$ in the range of 8.78 to 9.59. Nine of the ten WLQs have Mg II-based single-epoch virial SMBH masses in the Shen et al. (2011) SDSS DR7 catalog, and the other one has a C IV-based virial mass. The comparison of the masses are displayed in Figure 5. The $H\beta$ -based virial SMBH masses are systematically lower, by an average factor of 11.2 for our WLQs. Mg II-based virial SMBH masses for typical quasars are in general consistent with $H\beta$ -based ones (e.g., Shen et al. 2011; Bian et al. 2012; Tilton & Shull 2013; Maithil et al. 2022). However, most of our WLQs have weak Mg II lines, which likely hamper accurate line-profile measurements. Therefore, our $H\beta$ -based masses should be more reliable.

Adopting the L_{5100} bolometric correction prescription in Netzer (2019), we estimate the Eddington ratios with the following equation:

$$L_{\text{bol}}/L_{\text{Edd}} = [f(L) \times L_{5100}] / [1.5 \times 10^{38} M_{\text{BH}}/M_{\odot}], \quad (2)$$

where $f(L) = 40 \times [L_{5100}/10^{42} \text{ erg s}^{-1}]^{-0.2}$ is a luminosity-dependent bolometric correction factor (Table 1 of Netzer 2019). The resulting Eddington ratios are listed in Table 4. Our WLQs have large Eddington ratios in general; the median $L_{\text{bol}}/L_{\text{Edd}}$ value is 0.5 with an interquartile range of 0.4 to 0.7. For comparison, we computed $H\beta$ -based SMBH masses and Eddington ratios for the two comparison

samples using the measurements in Matthews et al. (2023). Eight of the 20 GW quasars have Mg II-based masses in the SDSS DR7 catalog, and another ten objects have C IV-based masses. For the other two quasars without DR7 masses, we adopted their C IV-based masses in the SDSS DR16 quasar catalog (Wu & Shen 2022). A comparison of the $H\beta$ -based SMBH masses and SDSS DR7 masses for the GW sample is included in Figure 5. The $H\beta$ -based virial SMBH masses are again systematically smaller. In Figure 6, we plot the M_{BH} versus $L_{\text{bol}}/L_{\text{Edd}}$ distributions for our sample and the comparison samples. There does not appear to be any significant difference between the M_{BH} or $L_{\text{bol}}/L_{\text{Edd}}$ distributions for our sample and the comparison samples. For the M_{BH} distributions of our sample and the GN sample, a K-S test yielded $P_{\text{null}} = 0.93$, and for the $L_{\text{bol}}/L_{\text{Edd}}$ distributions of these two samples, the P_{null} value is 0.74, both suggesting similar distributions. We also tested estimating SMBH masses for our WLQs based on their $H\alpha$ line profiles, following the approach in Greene & Ho (2005). The derived masses are comparable to the $H\beta$ -based estimates, and the result regarding the Eddington-ratio distributions remains the same.

We caution that there are substantial systematic uncertainties associated with the $L_{\text{bol}}/L_{\text{Edd}}$ estimates, especially for super-Eddington accreting quasars. The virial assumption might no longer be valid for super-Eddington accreting quasars due to the impact of the large radiation pressure and anisotropy of the ionizing radiation (e.g., Marconi et al. 2008, 2009; Netzer & Marziani 2010; Krause et al. 2011; Pancoast et al. 2014; Li et al. 2018). The radius–luminosity relation adopted in Equation 1 might break down in the super-Eddington regime (e.g., Hu et al. 2008; Wang et al. 2014b; Du et al. 2015; Du et al. 2016), and Du & Wang (2019) have proposed a new scaling relation with $R_{\text{Fe II}}$ being an additional parameter. We estimated M_{BH} based on this new scaling relation and the resulting M_{BH} values are smaller by a factor of ≈ 6.2 on average. Subsequently, the $L_{\text{bol}}/L_{\text{Edd}}$ values are larger by a factor of ≈ 6.2 on average. Substantial uncertainties might also come from the L_{bol} estimates for super-Eddington accreting quasars due to the uncertain extreme UV radiation (e.g., Castelló-Mor et al. 2016; Kubota & Done 2018). Moreover, the bolometric luminosity and the Eddington ratio are probably not good representatives of the accretion power in the super-Eddington regime, as a large fraction of the energy may be advected into the SMBH or be converted into the mechanical power of a wind (e.g., Wang et al. 2014a; Jiang et al. 2019). Therefore, a simple comparison of the $L_{\text{bol}}/L_{\text{Edd}}$ distributions for the WLQ sample and the GN sample does not provide strong constraints on the accretion power of WLQs compared to typical high- z quasars.

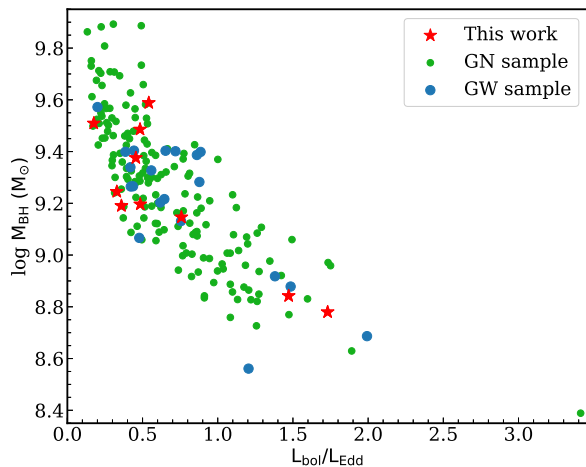


Figure 6. M_{BH} vs. $L_{\text{bol}}/L_{\text{Edd}}$ for our sample and the comparison samples. There is no significant difference between the M_{BH} or $L_{\text{bol}}/L_{\text{Edd}}$ distributions of these samples.

4. DISCUSSION

4.1. Thick Accretion Disk and Associated Outflow Scenario for WLQs

Our NIR spectroscopy of ten WLQs enlarges the limited samples of C IV-selected WLQs that have rest-frame optical spectroscopy (e.g., Shemmer et al. 2010; Wu et al. 2011; Plotkin et al. 2015; Shemmer & Lieber 2015; Ha et al. 2023). Based on VLT/X-Shooter spectra of six WLQs, Plotkin et al. (2015) found that statistically the $H\beta$ line emission in WLQs is not as exceptionally weak as for the C IV line emission. Our results (Section 3.1) reinforce this finding that the low-ionization lines are not strongly affected in these systems. Comparison with the GW sample (Table 3) also indicates that this archival WLQ sample shows typical $H\beta$ emission as well. These results are broadly consistent with the TDO obscuration scenario, where a soft ionizing continuum is produced after the TDO shielding and only the high-ionization BELR is significantly affected.

The most striking feature of the WLQ optical spectra appears to be the universally weak/absent [O III] emission, which was noticed before but did not attract much attention due to the limited samples available. As discussed in Section 3.1, such weak/absent [O III] emission is more likely an indicator of super-Eddington accretion, consistent with the TDO scenario. Being a narrow forbidden emission line, the [O III] $\lambda 5007$ line is produced in the galactic-scale narrow emission-line region (NELR), and its strength is believed to be correlated with the ionizing ($\gtrsim 35$ eV) luminosity received by the NELR. A positive correlation between the [O III] luminosity and the hard X-ray luminosity for active galactic nuclei (AGNs) across a broad luminosity range

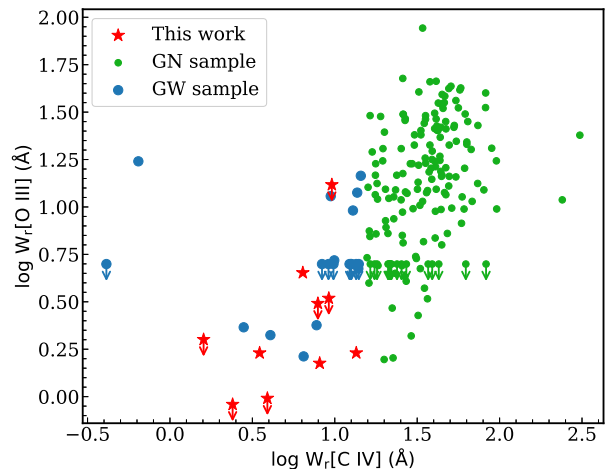


Figure 7. $\log W_r[\text{O III}]$ vs. $\log W_r[\text{C IV}]$ for our WLQ sample (red stars) and the comparison samples (blue and green dots). Upper limits are indicated by the downward arrows. The two REWs appear to be positively correlated, and the WLQ and GW quasars occupy the bottom left corner.

has been reported (e.g., Heckman et al. 2005; Panessa et al. 2006; Ueda et al. 2015). Since at least $\approx 50\%$ of the WLQs (i.e., those showing typical levels of X-ray emission) produce standard quasar SEDs from IR to X-ray, the weak [O III] emission should not be due to an intrinsically weak ionizing continuum.

There also appears to be a negative correlation, albeit with a large scatter, between the [O III] REW and quasar luminosity (e.g., Sulentic et al. 2004; Stern & Laor 2012; Coatman et al. 2019); one possible explanation is that the [O III] NELR cannot grow indefinitely with the ionizing luminosity as there will be no gas available to be ionized.⁵ However, in our case here, the WLQ and comparison samples have comparable luminosities (e.g., Figure 1). We ran a K-S test on the bolometric luminosity distributions of the WLQ and GN samples, and the resulting P_{null} value is 0.15, indicating no significant difference. Therefore, the weaker [O III] emission of the WLQs should not be due to higher luminosities than for the GN sample.

It has also been proposed that the [O III] emission strength (and some of the Eigenvector 1 correlations) could be mainly explained by orientation effects (e.g., Bisogni et al. 2017). In this scenario, the [O III] emission is isotropic while the disk continuum emission is orientation dependent. Thus a face-on view would result in a smaller [O III] REW than that in

⁵ However, we note that the inner boundary for the [O III] NELR might still be fairly compact even when the luminosity is high (e.g., ~ 100 pc for an ionizing luminosity of 10^{47} erg s^{-1}), according to the computation results in Figure 6 of Stern et al. (2014).

an edge-on view, and the weak [O III] emission of the WLQs could be explained if they preferentially have small inclination angles. However, the significant positive correlation between Eigenvector 1 and [O III] luminosity argues against an orientation dominated dependence (Figure 8 and Section 4.1 of Boroson & Green 1992). Moreover, the WLQs were selected based on the weak C IV emission, while in this orientation scenario, broad emission-line strength does not have an orientation dependence. It thus appears impossible to select a sample of face-on quasars with the C IV REW criterion. Another argument against this explanation is based on the $\approx 30 - 50\%$ of X-ray weak WLQs observed (Section 1). The X-ray weakness is likely attributed to X-ray absorption, but it is hard to explain such significant X-ray absorption with face-on views.

In Figure 7, we show the WLQ, GW, and GN samples in the $\log W_r[\text{O III}]$ vs. $\log W_r[\text{C IV}]$ plane. It is clear that the WLQ and GW quasars are located in the bottom left corner, with both weak [O III] and C IV emission. The two REWs appear to be positively correlated, with a Spearman rank-order correlation coefficient of $\rho = 0.556$. Similar to the [O III] emission, the strength of the C IV emission also reflects the ionizing ($\gtrsim 48$ eV) luminosity received by the C IV BELR. In the TDO scenario for WLQs, the equatorial C IV BELR is shielded by the TDO, leading to the weak line emission. A similar mechanism might work for the weak [O III] emission in WLQs. The ionizing extreme UV and X-ray radiation is confined to the funnel region in the configuration of a geometrically thick accretion disk (see Figure 1 of Ni et al. 2018), and thus the [O III] NELR has a small covering factor (i.e., a small solid angle for the ionization cone; e.g., Wang et al. 2014a), resulting in the weak line emission. Larger samples of WLQs with [O III] measurements will help to constrain statistically the covering factors and photoionization conditions of the NELRs (e.g., Baskin & Laor 2005).

Strong optical Fe II emission appears to be another important feature, although the contrast between WLQs and typical quasars is not as high as that for the [O III] emission (Table 3). This feature also suggests high accretion rates in general, and thus it is consistent with the TDO scenario. Although many studies have suggested a positive correlation between Fe II emission strength and Eddington ratio, there is no clear understanding of the underlying physics, mainly due to the complex excitation mechanisms and the poorly constrained location for the Fe II emission (e.g., Dong et al. 2011; Marinello et al. 2016). One proposed interpretation is that only high-density clouds are gravitationally bound in super-Eddington accreting systems, which produce strong Fe emission due to radiative transfer effects (Sameshima et al. 2011). Another possibility is that super-Eddington accreting AGNs might have high metal

contents (e.g., Śniegowska et al. 2021; Dias dos Santos et al. 2024; Marziani et al. 2024).

Overall, the optical spectral properties of our systematically selected sample of WLQs provide further support to the TDO scenario. With the $H\beta$ emission-line measurements, we are able to estimate more reliably the SMBH masses. However, as discussed in Section 3.2, extra caution is needed when assessing the accretion power for super-Eddington accretion with the Eddington-ratio parameter.

WLQs also display exceptional X-ray properties. Four of our sources have previous X-ray coverage from Wu et al. (2012), Luo et al. (2015), or Ni et al. (2022). Two of them show typical levels of X-ray emission (X-ray normal) as expected from the $\alpha_{\text{OX}}-L_{2500 \text{ \AA}}$ relation, while the other two were not detected in the Chandra observations and are X-ray weak by factors of > 10.1 and > 27.4 compared to the $\alpha_{\text{OX}}-L_{2500 \text{ \AA}}$ relation. The basic X-ray and optical emission-line properties for these four WLQs are listed in Table 5. Under the TDO scenario, X-ray normal and X-ray weak WLQs are intrinsically similar, but the X-ray weak ones are viewed at larger inclination angles with TDO obscuration along the line of sight. Our sample of four objects is too small for statistical comparisons, but among the emission-line properties studies here, the X-ray weak WLQs appear to have broader $H\beta$ lines, consistent with the expectation from larger inclination angles given a flattened BELR geometry (e.g., Wills & Browne 1986; Runnoe et al. 2013; Shen & Ho 2014). We caution that the $H\beta$ width should have considerable object-to-object scatter, and statistical assessment on a larger sample is needed to confirm such a difference.

Another interesting question to explore is the connection between WLQs and super-Eddington accreting quasars in general. For example, are WLQs special among super-Eddington accreting quasars? There are small samples of super-Eddington accreting quasars selected based on their Eddington ratios, luminosities, X-ray properties (e.g., steep spectral shapes), and/or Eigenvector 1 parameters (e.g., Nardini et al. 2019; Liu et al. 2021; Lusso et al. 2021; Laurenti et al. 2022). These objects share many similarities with WLQs in terms of their SEDs (typical IR–UV quasar SEDs), X-ray properties (sometimes X-ray weak and X-ray variable), and optical spectral properties (as discussed in this study). Some of these quasars indeed show weak C IV emission lines and could be considered WLQs, but some show nominal levels of C IV emission. Thus super-Eddington accreting quasars are unlikely all WLQs. Under the TDO scenario, the weakness of C IV line is controlled by the TDO shielding. The covering factor and/or column density of the TDO in a strong C IV emitter are thus lower than those of a WLQ; WLQs are probably extremely super-Eddington accreting with high-covering-factor high-density TDOs. Ob-

servationally, one could test this hypothesis via comparing the fraction of X-ray weak quasars and the X-ray weakness factors between these two populations. Examining these two populations in the Eigenvector 1 parameter space might also provide insights.

4.2. Candidate Extreme [O III] $\lambda 5007$ Outflows in SDSS J153714.26+271611.6

The spectrum of SDSS J153714.26+271611.6 (J1537 hereafter) suggests the presence of blueshifted broad [O III] emission lines (Figure 2). Two broad components are required to fit the spectrum, with FWHMs of $\approx 1910 \pm 140$ and $\approx 2900 \pm 260$ km s⁻¹. If these two components are the [O III] $\lambda 4959$ and $\lambda 5007$ doublet, the blueshifts are ≈ 500 – 2000 km s⁻¹. However, the line fluxes do not follow the 1 : 3 ratio, suggesting that these might both be the [O III] $\lambda 5007$ line but at different blueshifts. The blueshifts are thus $\approx 500 \pm 170$ and $\approx 4900 \pm 140$ km s⁻¹.

There is no previous report of blueshifted broad [O III] emission lines in WLQs, and there are only a limited number of such cases in quasars (e.g., Brusa et al. 2015, 2016; Zakamska et al. 2016; Bischetti et al. 2017; Xu et al. 2020; Fukuchi et al. 2023). These lines suggest strong [O III] outflows in the host galaxy, and they provide strong evidence for quasar feedback. Super-Eddington accreting quasars are expected to produce powerful accretion-disk winds (e.g., Giustini & Proga 2019; Jiang et al. 2019), which may develop into massive galactic-scale outflows. The [O III] blueshifts in J1537 indeed appear higher than those discovered in other quasars (e.g., Zakamska et al. 2016). Under the TDO scenario, the [O III] ionizing cone has a small solid angle. Thus blueshifted lines indicate a small inclination angle. J1537 shows a nominal level of X-ray emission (Table 5), which also indicates a relatively small inclination angle. Such an inclination-angle constraint might also limit the occurrence of blueshifted broad [O III] lines in WLQs in general. Nevertheless, we caution that the P200/TSpec spectrum has a limited SNR, and there might also be contamination from additional Fe II emission around [O III] (e.g., Kovačević et al. 2010; Bischetti et al. 2017). In certain instances, these lines can be incorrectly identified as [O III] emission, even though they don't align well with the characteristics of these two broad components. Therefore, we consider J1537 a candidate for containing extreme [O III] $\lambda 5007$ outflows. Higher quality NIR spectra are required to confirm the presence of these extreme blueshifted broad [O III] lines and study their kinematics.

5. SUMMARY

In this paper, we present systematic investigations of the optical emission-line properties for a sample of $z \sim 2$ WLQs observed with P200/TSpec. The final sample contains ten WLQs with C IV REWs < 15 Å (nine having C IV

REWs < 10 Å). Four sources have previous X-ray coverage. For comparison, we constructed a typical quasar (GN) sample containing 168 high-redshift ($z \approx 1.5 - 3.5$) quasars with GNIRS-DQS NIR spectra (Matthews et al. 2021). The 20 archival WLQs in the Matthews et al. (2023) GNIRS-DQS catalog constitute the GW comparison sample; the emission-line properties of our sample and the GW sample are consistent overall.

The emission-line features we examined include the H β REW, H β FWHM, [O III] REW, and $R_{\text{Fe II}}$ (Figure 3). We confirmed the previous finding that the WLQ H β lines, as a major low-ionization line, are not significantly weak compared to typical quasars. This result supports the soft ionizing continuum scenario where only the high-ionization BELR is strongly affected, leading to the exceptionally weak C IV emission. There is no significant difference between the H β FWHM distributions either. The most prominent feature of the WLQ optical spectra is the universally weak/absent [O III] emission. WLQs also display stronger optical Fe II emission ($R_{\text{Fe II}}$) than typical quasars. Weak [O III] emission and strong Fe II emission suggest high accretion rates for the WLQs considering the Eigenvector 1 correlations. See Section 3.1.

We derived H β -based single-epoch virial SMBH masses and Eddington ratios for our objects. These are massive SMBHs ($\sim 10^9 M_{\odot}$) with large Eddington ratios (median $L_{\text{bol}}/L_{\text{Edd}} = 0.5$). There is no significant difference between the M_{BH} or $L_{\text{bol}}/L_{\text{Edd}}$ distributions for our sample and the comparison samples, but extra caution is needed for the interpretation. See Section 3.2.

Our results provide further support to the TDO scenario, where WLQs are super-Eddington accreting and the weak high-ionization UV emission lines are produced due to a soft ionizing continuum from TDO shielding. This scenario can also explain the remarkable X-ray properties and other multiwavelength properties of WLQs. The candidate extreme [O III] $\lambda 5007$ outflows (blueshifts of ≈ 500 and ≈ 4900 km s⁻¹) in J1537 might connect to the small-scale TDO. See Section 4.

WLQs appear to be a unique quasar population that is able to provide important clues about SMBH accretion, accretion-driven outflows, and the nuclear gaseous environment. The current samples of C IV-selected WLQs with rest-frame optical spectra are still small, and they lack systematic selections or spectral analyses. NIR spectroscopy of a large sample uniformly selected from the SDSS quasar catalog (e.g., DR16; Wu & Shen 2022), aided with X-ray coverage, will be helpful for constraining more reliably their nature. We note that although Ni et al. (2022) has composed a well-defined sample of 32 WLQs with good X-ray coverage, the redshifts for a large fraction of these objects fall outside the observing window for ground observations due

Table 5. X-ray and Optical Emission-Line Properties

Source Name (SDSS J)	α_{OX}	$\Delta\alpha_{\text{OX}}$	f_{weak}	H β REW (\AA)	[O III] REW (\AA)	Fe II REW (\AA)	H β FWHM (km s^{-1})
X-ray Weak Quasars							
153412.68+503405.3	< -2.11	< -0.39	> 10.1	91.1 ± 1.5	< 3.3	59 ± 3	5040 ± 65
134601.28+585820.2	< -2.22	< -0.55	> 27.4	17.3 ± 1.3	< 0.91	56 ± 5	6990 ± 1100
X-ray Normal Quasars							
153714.26+271611.6	-1.82	-0.06	1.4	24.9 ± 0.4	< 3.1	50 ± 2	2500 ± 1200
161245.68+511816.9	-1.67	0.02	0.9	25.4 ± 1.4	< 2.0	70 ± 4	4870 ± 360

NOTE—The X-ray properties are adopted from Wu et al. (2012), Luo et al. (2015), or Ni et al. (2022). $\Delta\alpha_{\text{OX}}$ is defined as the difference between the observed α_{OX} value and the one expected from the $\alpha_{\text{OX}}-L_{2500 \text{ \AA}}$ relation ($\Delta\alpha_{\text{OX}} = \alpha_{\text{OX}} - \alpha_{\text{OX,exp}}$), and $f_{\text{weak}} = 10^{-\Delta\alpha_{\text{OX}}/0.383} \approx 403^{-\Delta\alpha_{\text{OX}}}$. The emission-line properties are the same as those in Table 2.

to telluric absorption. NIR spectroscopy from JWST would be very helpful in this regard.

We thank J. M. Wang for helpful discussions. Y.C. and B.L. acknowledge financial support from the National Natural Science Foundation of China grants 11991053 and 11991050, China Manned Space Project grants NO. CMS-CSST-2021-A05 and NO. CMS-CSST-2021-A06, and CNSA program D050102. WNB acknowledges the Eberly Endowment at Penn State.

This research uses data obtained through the Telescope Access Program (TAP), which has been funded by the Strategic Priority Research Program “The Emergence of Cosmological Structures” (Grant No. XBD09000000), National Astronomical Observatories, Chinese Academy of Sciences, and the Special Fund for Astronomy from the Ministry of Finance. Observations obtained with the Hale Telescope at Palomar Observatory were obtained as part of an agreement between the National Astronomical Observatories, Chinese Academy of Sciences, and the California Institute of Technology.

REFERENCES

- Abazajian, K. N., Adelman-McCarthy, J. K., Agüeros, M. A., et al. 2009, *ApJS*, 182, 543, doi: [10.1088/0067-0049/182/2/543](https://doi.org/10.1088/0067-0049/182/2/543)
- Bañados, E., Venemans, B. P., Decarli, R., et al. 2016, *ApJS*, 227, 11, doi: [10.3847/0067-0049/227/1/11](https://doi.org/10.3847/0067-0049/227/1/11)
- Baskin, A., & Laor, A. 2005, *MNRAS*, 356, 1029, doi: [10.1111/j.1365-2966.2004.08525.x](https://doi.org/10.1111/j.1365-2966.2004.08525.x)
- Becker, R. H., White, R. L., & Helfand, D. J. 1995, *ApJ*, 450, 559, doi: [10.1086/176166](https://doi.org/10.1086/176166)
- Bentz, M. C., Peterson, B. M., Netzer, H., Pogge, R. W., & Vestergaard, M. 2009, *ApJ*, 697, 160, doi: [10.1088/0004-637X/697/1/160](https://doi.org/10.1088/0004-637X/697/1/160)
- Bian, W., Fang, L.-L., Huang, K.-L., & Wang, J.-M. 2012, *MNRAS*, 427, 2881, doi: [10.1111/j.1365-2966.2012.22123.x](https://doi.org/10.1111/j.1365-2966.2012.22123.x)
- Bischetti, M., Piconcelli, E., Vietri, G., et al. 2017, *A&A*, 598, A122, doi: [10.1051/0004-6361/201629301](https://doi.org/10.1051/0004-6361/201629301)
- Bisogni, S., Marconi, A., & Risaliti, G. 2017, *MNRAS*, 464, 385, doi: [10.1093/mnras/stw2324](https://doi.org/10.1093/mnras/stw2324)
- Boroson, T. A., & Green, R. F. 1992, *ApJS*, 80, 109, doi: [10.1086/191661](https://doi.org/10.1086/191661)
- Brusa, M., Bongiorno, A., Cresci, G., et al. 2015, *MNRAS*, 446, 2394, doi: [10.1093/mnras/stu2117](https://doi.org/10.1093/mnras/stu2117)
- Brusa, M., Perna, M., Cresci, G., et al. 2016, *A&A*, 588, A58, doi: [10.1051/0004-6361/201527900](https://doi.org/10.1051/0004-6361/201527900)
- Castelló-Mor, N., Netzer, H., & Kaspi, S. 2016, *MNRAS*, 458, 1839, doi: [10.1093/mnras/stw445](https://doi.org/10.1093/mnras/stw445)
- Coatman, L., Hewett, P. C., Banerji, M., et al. 2017, *MNRAS*, 465, 2120, doi: [10.1093/mnras/stw2797](https://doi.org/10.1093/mnras/stw2797)
- , 2019, *MNRAS*, 486, 5335, doi: [10.1093/mnras/stz1167](https://doi.org/10.1093/mnras/stz1167)
- Condon, J. J., Cotton, W. D., Greisen, E. W., et al. 1998, *AJ*, 115, 1693, doi: [10.1086/300337](https://doi.org/10.1086/300337)
- Cushing, M., Vacca, B., & Rayner, J. 2014, Spextool: Spectral EXtraction tool. <http://ascl.net/1404.017>
- Denney, K. D. 2012, *ApJ*, 759, 44, doi: [10.1088/0004-637X/759/1/44](https://doi.org/10.1088/0004-637X/759/1/44)
- Diamond-Stanic, A. M., Fan, X., Brandt, W. N., et al. 2009, *ApJ*, 699, 782, doi: [10.1088/0004-637X/699/1/782](https://doi.org/10.1088/0004-637X/699/1/782)
- Dias dos Santos, D., Panda, S., Rodríguez-Ardila, A., & Marinello, M. 2024, *Physics*, 6, 177, doi: [10.3390/physics6010013](https://doi.org/10.3390/physics6010013)

- Dix, C., Matthews, B., Shemmer, O., et al. 2023, *ApJ*, 950, 96, doi: [10.3847/1538-4357/acd04b](https://doi.org/10.3847/1538-4357/acd04b)
- Dong, X.-B., Wang, J.-G., Ho, L. C., et al. 2011, *ApJ*, 736, 86, doi: [10.1088/0004-637X/736/2/86](https://doi.org/10.1088/0004-637X/736/2/86)
- Du, P., & Wang, J.-M. 2019, *ApJ*, 886, 42, doi: [10.3847/1538-4357/ab4908](https://doi.org/10.3847/1538-4357/ab4908)
- Du, P., Wang, J.-M., Hu, C., et al. 2016, *ApJL*, 818, L14, doi: [10.3847/2041-8205/818/L14](https://doi.org/10.3847/2041-8205/818/L14)
- Du, P., Hu, C., Lu, K.-X., et al. 2014, *ApJ*, 782, 45, doi: [10.1088/0004-637X/782/1/45](https://doi.org/10.1088/0004-637X/782/1/45)
- Du, P., Hu, C., Lu, K.-X., et al. 2015, *ApJ*, 806, 22, doi: [10.1088/0004-637X/806/1/22](https://doi.org/10.1088/0004-637X/806/1/22)
- Eilers, A.-C., Simcoe, R. A., Yue, M., et al. 2023, *ApJ*, 950, 68, doi: [10.3847/1538-4357/acd776](https://doi.org/10.3847/1538-4357/acd776)
- Fan, X., Strauss, M. A., Gunn, J. E., et al. 1999, *ApJL*, 526, L57, doi: [10.1086/312382](https://doi.org/10.1086/312382)
- Feigelson, E. D., & Nelson, P. I. 1985, *ApJ*, 293, 192, doi: [10.1086/163225](https://doi.org/10.1086/163225)
- Fitzpatrick, E. L. 1999, *PASP*, 111, 63, doi: [10.1086/316293](https://doi.org/10.1086/316293)
- Fukuchi, H., Ichikawa, K., Akiyama, M., et al. 2023, arXiv e-prints, arXiv:2303.05605, doi: [10.48550/arXiv.2303.05605](https://doi.org/10.48550/arXiv.2303.05605)
- Gallagher, S. C., Brandt, W. N., Chartas, G., & Garmire, G. P. 2002, *ApJ*, 567, 37, doi: [10.1086/338485](https://doi.org/10.1086/338485)
- Gallagher, S. C., Brandt, W. N., Chartas, G., et al. 2006, *ApJ*, 644, 709, doi: [10.1086/503762](https://doi.org/10.1086/503762)
- Giustini, M., & Proga, D. 2019, *A&A*, 630, A94, doi: [10.1051/0004-6361/201833810](https://doi.org/10.1051/0004-6361/201833810)
- Greene, J. E., & Ho, L. C. 2005, *ApJ*, 630, 122, doi: [10.1086/431897](https://doi.org/10.1086/431897)
- Guo, H., Liu, X., Shen, Y., et al. 2019, *MNRAS*, 482, 3288, doi: [10.1093/mnras/sty2920](https://doi.org/10.1093/mnras/sty2920)
- Guo, H., Shen, Y., & Wang, S. 2018, PyQSOFit: Python code to fit the spectrum of quasars, *Astrophysics Source Code Library*. <http://ascl.net/1809.008>
- Ha, T., Dix, C., Matthews, B. M., et al. 2023, *ApJ*, 950, 97, doi: [10.3847/1538-4357/acd04d](https://doi.org/10.3847/1538-4357/acd04d)
- Heckman, T. M., Ptak, A., Hornschemeier, A., & Kauffmann, G. 2005, *ApJ*, 634, 161, doi: [10.1086/491665](https://doi.org/10.1086/491665)
- Herter, T. L., Henderson, C. P., Wilson, J. C., et al. 2008, in *Society of Photo-Optical Instrumentation Engineers (SPIE) Conference Series*, Vol. 7014, *Ground-based and Airborne Instrumentation for Astronomy II*, ed. I. S. McLean & M. M. Casali, 70140X, doi: [10.1117/12.789660](https://doi.org/10.1117/12.789660)
- Hewett, P. C., & Wild, V. 2010, *MNRAS*, 405, 2302, doi: [10.1111/j.1365-2966.2010.16648.x](https://doi.org/10.1111/j.1365-2966.2010.16648.x)
- Hu, C., Wang, J.-M., Ho, L. C., et al. 2008, *ApJ*, 687, 78, doi: [10.1086/591838](https://doi.org/10.1086/591838)
- Jiang, Y.-F., Stone, J. M., & Davis, S. W. 2019, *ApJ*, 880, 67, doi: [10.3847/1538-4357/ab29ff](https://doi.org/10.3847/1538-4357/ab29ff)
- Kaspi, S., Smith, P. S., Netzer, H., et al. 2000, *ApJ*, 533, 631, doi: [10.1086/308704](https://doi.org/10.1086/308704)
- Kellermann, K. I., Sramek, R., Schmidt, M., Shaffer, D. B., & Green, R. 1989, *AJ*, 98, 1195, doi: [10.1086/115207](https://doi.org/10.1086/115207)
- Kovačević, J., Popović, L. Č., & Dimitrijević, M. S. 2010, *ApJS*, 189, 15, doi: [10.1088/0067-0049/189/1/15](https://doi.org/10.1088/0067-0049/189/1/15)
- Kratzer, R. M., & Richards, G. T. 2015, *AJ*, 149, 61, doi: [10.1088/0004-6256/149/2/61](https://doi.org/10.1088/0004-6256/149/2/61)
- Krause, M., Burkert, A., & Schartmann, M. 2011, *MNRAS*, 411, 550, doi: [10.1111/j.1365-2966.2010.17698.x](https://doi.org/10.1111/j.1365-2966.2010.17698.x)
- Kubota, A., & Done, C. 2018, *MNRAS*, 480, 1247, doi: [10.1093/mnras/sty1890](https://doi.org/10.1093/mnras/sty1890)
- Lane, R. A., Shemmer, O., Diamond-Stanic, A. M., et al. 2011, *ApJ*, 743, 163, doi: [10.1088/0004-637X/743/2/163](https://doi.org/10.1088/0004-637X/743/2/163)
- Laurenti, M., Piconcelli, E., Zappacosta, L., et al. 2022, *A&A*, 657, A57, doi: [10.1051/0004-6361/202141829](https://doi.org/10.1051/0004-6361/202141829)
- Lavalley, M., Isobe, T., & Feigelson, E. 1992, in *Astronomical Society of the Pacific Conference Series*, Vol. 25, *Astronomical Data Analysis Software and Systems I*, ed. D. M. Worrall, C. Biemesderfer, & J. Barnes, 245
- Leighly, K. M., Halpern, J. P., Jenkins, E. B., & Casebeer, D. 2007, *ApJS*, 173, 1, doi: [10.1086/519768](https://doi.org/10.1086/519768)
- Li, Y.-R., Songsheng, Y.-Y., Qiu, J., et al. 2018, *ApJ*, 869, 137, doi: [10.3847/1538-4357/aace6b](https://doi.org/10.3847/1538-4357/aace6b)
- Liu, H., Luo, B., Brandt, W. N., et al. 2021, *ApJ*, 910, 103, doi: [10.3847/1538-4357/abe37f](https://doi.org/10.3847/1538-4357/abe37f)
- Liu, H., Luo, B., Brandt, W. N., et al. 2022, *ApJ*, 930, 53, doi: [10.3847/1538-4357/ac6265](https://doi.org/10.3847/1538-4357/ac6265)
- Luo, B., Brandt, W. N., Hall, P. B., et al. 2015, *ApJ*, 805, 122, doi: [10.1088/0004-637X/805/2/122](https://doi.org/10.1088/0004-637X/805/2/122)
- Lusso, E., Nardini, E., Bisogni, S., et al. 2021, *A&A*, 653, A158, doi: [10.1051/0004-6361/202141356](https://doi.org/10.1051/0004-6361/202141356)
- Maithil, J., Brotherton, M. S., Shemmer, O., et al. 2022, *MNRAS*, 515, 491, doi: [10.1093/mnras/stac1748](https://doi.org/10.1093/mnras/stac1748)
- Maoz, D., Netzer, H., Mazeh, T., et al. 1991, *ApJ*, 367, 493, doi: [10.1086/169646](https://doi.org/10.1086/169646)
- Marconi, A., Axon, D. J., Maiolino, R., et al. 2008, *ApJ*, 678, 693, doi: [10.1086/529360](https://doi.org/10.1086/529360)
- . 2009, *ApJL*, 698, L103, doi: [10.1088/0004-637X/698/2/L103](https://doi.org/10.1088/0004-637X/698/2/L103)
- Marinello, M., Rodríguez-Ardila, A., Garcia-Rissmann, A., Sigut, T. A. A., & Pradhan, A. K. 2016, *ApJ*, 820, 116, doi: [10.3847/0004-637X/820/2/116](https://doi.org/10.3847/0004-637X/820/2/116)
- Marziani, P., Floris, A., Deconto-Machado, A., et al. 2024, *Physics*, 6, 216, doi: [10.3390/physics6010016](https://doi.org/10.3390/physics6010016)
- Matthews, B. M., Shemmer, O., Dix, C., et al. 2021, *ApJS*, 252, 15, doi: [10.3847/1538-4365/abc705](https://doi.org/10.3847/1538-4365/abc705)
- Matthews, B. M., Dix, C., Shemmer, O., et al. 2023, *ApJ*, 950, 95, doi: [10.3847/1538-4357/acd04c](https://doi.org/10.3847/1538-4357/acd04c)
- Miniutti, G., Brandt, W. N., Schneider, D. P., et al. 2012, *MNRAS*, 425, 1718, doi: [10.1111/j.1365-2966.2012.21648.x](https://doi.org/10.1111/j.1365-2966.2012.21648.x)

- Nardini, E., Lusso, E., Risaliti, G., et al. 2019, *A&A*, 632, A109, doi: [10.1051/0004-6361/201936911](https://doi.org/10.1051/0004-6361/201936911)
- Netzer, H. 2019, *MNRAS*, 488, 5185, doi: [10.1093/mnras/stz2016](https://doi.org/10.1093/mnras/stz2016)
- Netzer, H., & Marziani, P. 2010, *ApJ*, 724, 318, doi: [10.1088/0004-637X/724/1/318](https://doi.org/10.1088/0004-637X/724/1/318)
- Ni, Q., Brandt, W. N., Luo, B., et al. 2018, *MNRAS*, 480, 5184, doi: [10.1093/mnras/sty1989](https://doi.org/10.1093/mnras/sty1989)
- Ni, Q., Brandt, W. N., Yi, W., et al. 2020, *ApJL*, 889, L37, doi: [10.3847/2041-8213/ab6d78](https://doi.org/10.3847/2041-8213/ab6d78)
- Ni, Q., Brandt, W. N., Luo, B., et al. 2022, *MNRAS*, 511, 5251, doi: [10.1093/mnras/stac394](https://doi.org/10.1093/mnras/stac394)
- Pancoast, A., Brewer, B. J., Treu, T., et al. 2014, *MNRAS*, 445, 3073, doi: [10.1093/mnras/stu1419](https://doi.org/10.1093/mnras/stu1419)
- Panessa, F., Bassani, L., Cappi, M., et al. 2006, *A&A*, 455, 173, doi: [10.1051/0004-6361:20064894](https://doi.org/10.1051/0004-6361:20064894)
- Paul, J. D., Plotkin, R. M., Shemmer, O., et al. 2022, *ApJ*, 929, 78, doi: [10.3847/1538-4357/ac5bd6](https://doi.org/10.3847/1538-4357/ac5bd6)
- Perna, M., Brusa, M., Cresci, G., et al. 2015, *A&A*, 574, A82, doi: [10.1051/0004-6361/201425035](https://doi.org/10.1051/0004-6361/201425035)
- Peterson, B. M., Balonek, T. J., Barker, E. S., et al. 1991, *ApJ*, 368, 119, doi: [10.1086/169675](https://doi.org/10.1086/169675)
- Planck Collaboration, Aghanim, N., Akrami, Y., et al. 2020, *A&A*, 641, A6, doi: [10.1051/0004-6361/201833910](https://doi.org/10.1051/0004-6361/201833910)
- Plotkin, R. M., Anderson, S. F., Brandt, W. N., et al. 2010, *AJ*, 139, 390, doi: [10.1088/0004-6256/139/2/390](https://doi.org/10.1088/0004-6256/139/2/390)
- Plotkin, R. M., Shemmer, O., Trakhtenbrot, B., et al. 2015, *ApJ*, 805, 123, doi: [10.1088/0004-637X/805/2/123](https://doi.org/10.1088/0004-637X/805/2/123)
- Pu, X., Luo, B., Brandt, W. N., et al. 2020, *ApJ*, 900, 141, doi: [10.3847/1538-4357/abacc5](https://doi.org/10.3847/1538-4357/abacc5)
- Runnoe, J. C., Brotherton, M. S., Shang, Z., Wills, B. J., & DiPompeo, M. A. 2013, *MNRAS*, 429, 135, doi: [10.1093/mnras/sts322](https://doi.org/10.1093/mnras/sts322)
- Sameshima, H., Kawara, K., Matsuoka, Y., et al. 2011, *MNRAS*, 410, 1018, doi: [10.1111/j.1365-2966.2010.17498.x](https://doi.org/10.1111/j.1365-2966.2010.17498.x)
- Schlegel, D. J., Finkbeiner, D. P., & Davis, M. 1998, *ApJ*, 500, 525, doi: [10.1086/305772](https://doi.org/10.1086/305772)
- Schneider, D. P., Richards, G. T., Hall, P. B., et al. 2010, *AJ*, 139, 2360, doi: [10.1088/0004-6256/139/6/2360](https://doi.org/10.1088/0004-6256/139/6/2360)
- Shemmer, O., Brandt, W. N., Anderson, S. F., et al. 2009, *ApJ*, 696, 580, doi: [10.1088/0004-637X/696/1/580](https://doi.org/10.1088/0004-637X/696/1/580)
- Shemmer, O., & Lieber, S. 2015, *ApJ*, 805, 124, doi: [10.1088/0004-637X/805/2/124](https://doi.org/10.1088/0004-637X/805/2/124)
- Shemmer, O., Trakhtenbrot, B., Anderson, S. F., et al. 2010, *ApJL*, 722, L152, doi: [10.1088/2041-8205/722/2/L152](https://doi.org/10.1088/2041-8205/722/2/L152)
- Shen, Y. 2021, *ApJ*, 921, 70, doi: [10.3847/1538-4357/ac1ce4](https://doi.org/10.3847/1538-4357/ac1ce4)
- Shen, Y., & Ho, L. C. 2014, *Nature*, 513, 210, doi: [10.1038/nature13712](https://doi.org/10.1038/nature13712)
- Shen, Y., & Liu, X. 2012, *ApJ*, 753, 125, doi: [10.1088/0004-637X/753/2/125](https://doi.org/10.1088/0004-637X/753/2/125)
- Shen, Y., Richards, G. T., Strauss, M. A., et al. 2011, *ApJS*, 194, 45, doi: [10.1088/0067-0049/194/2/45](https://doi.org/10.1088/0067-0049/194/2/45)
- Śniegowska, M., Marziani, P., Czerny, B., et al. 2021, *ApJ*, 910, 115, doi: [10.3847/1538-4357/abe1c8](https://doi.org/10.3847/1538-4357/abe1c8)
- Steffen, A. T., Strateva, I., Brandt, W. N., et al. 2006, *AJ*, 131, 2826, doi: [10.1086/503627](https://doi.org/10.1086/503627)
- Stern, J., & Laor, A. 2012, *MNRAS*, 426, 2703, doi: [10.1111/j.1365-2966.2012.21772.x](https://doi.org/10.1111/j.1365-2966.2012.21772.x)
- Stern, J., Laor, A., & Baskin, A. 2014, *MNRAS*, 438, 901, doi: [10.1093/mnras/stt1843](https://doi.org/10.1093/mnras/stt1843)
- Suberlak, K. L., Ivezić, Ž., & MacLeod, C. 2021, *ApJ*, 907, 96, doi: [10.3847/1538-4357/abc698](https://doi.org/10.3847/1538-4357/abc698)
- Sulentic, J. W., Stirpe, G. M., Marziani, P., et al. 2004, *A&A*, 423, 121, doi: [10.1051/0004-6361:20035912](https://doi.org/10.1051/0004-6361:20035912)
- Sulentic, J. W., Zwitter, T., Marziani, P., & Dultzin-Hacyan, D. 2000, *ApJL*, 536, L5, doi: [10.1086/312717](https://doi.org/10.1086/312717)
- Tilton, E. M., & Shull, J. M. 2013, *ApJ*, 774, 67, doi: [10.1088/0004-637X/774/1/67](https://doi.org/10.1088/0004-637X/774/1/67)
- Ueda, Y., Hashimoto, Y., Ichikawa, K., et al. 2015, *ApJ*, 815, 1, doi: [10.1088/0004-637X/815/1/1](https://doi.org/10.1088/0004-637X/815/1/1)
- Vacca, W. D., Cushing, M. C., & Rayner, J. T. 2003, *PASP*, 115, 389, doi: [10.1086/346193](https://doi.org/10.1086/346193)
- Vanden Berk, D. E., Richards, G. T., Bauer, A., et al. 2001, *AJ*, 122, 549, doi: [10.1086/321167](https://doi.org/10.1086/321167)
- Vietri, G., Piconcelli, E., Bischetti, M., et al. 2018, *A&A*, 617, A81, doi: [10.1051/0004-6361/201732335](https://doi.org/10.1051/0004-6361/201732335)
- Wang, J.-M., Qiu, J., Du, P., & Ho, L. C. 2014a, *ApJ*, 797, 65, doi: [10.1088/0004-637X/797/1/65](https://doi.org/10.1088/0004-637X/797/1/65)
- Wang, J.-M., Du, P., Hu, C., et al. 2014b, *ApJ*, 793, 108, doi: [10.1088/0004-637X/793/2/108](https://doi.org/10.1088/0004-637X/793/2/108)
- Wills, B. J., & Browne, I. W. A. 1986, *ApJ*, 302, 56, doi: [10.1086/163973](https://doi.org/10.1086/163973)
- Wolf, C., Hon, W. J., Bian, F., et al. 2020, *MNRAS*, 491, 1970, doi: [10.1093/mnras/stz2955](https://doi.org/10.1093/mnras/stz2955)
- Wu, J., Brandt, W. N., Anderson, S. F., et al. 2012, *ApJ*, 747, 10, doi: [10.1088/0004-637X/747/1/10](https://doi.org/10.1088/0004-637X/747/1/10)
- Wu, J., Brandt, W. N., Hall, P. B., et al. 2011, *ApJ*, 736, 28, doi: [10.1088/0004-637X/736/1/28](https://doi.org/10.1088/0004-637X/736/1/28)
- Wu, Q., & Shen, Y. 2022, *ApJS*, 263, 42, doi: [10.3847/1538-4365/ac9ead](https://doi.org/10.3847/1538-4365/ac9ead)
- Wu, X.-B., Wang, F., Fan, X., et al. 2015, *Nature*, 518, 512, doi: [10.1038/nature14241](https://doi.org/10.1038/nature14241)
- Xu, X., Zakamska, N. L., Arav, N., Miller, T., & Benn, C. 2020, *MNRAS*, 495, 305, doi: [10.1093/mnras/staa1142](https://doi.org/10.1093/mnras/staa1142)
- York, D. G., Adelman, J., Anderson, John E., J., et al. 2000, *AJ*, 120, 1579, doi: [10.1086/301513](https://doi.org/10.1086/301513)
- Zakamska, N. L., Hamann, F., Pâris, I., et al. 2016, *MNRAS*, 459, 3144, doi: [10.1093/mnras/stw718](https://doi.org/10.1093/mnras/stw718)
- Zappacosta, L., Piconcelli, E., Giustini, M., et al. 2020, *A&A*, 635, L5, doi: [10.1051/0004-6361/201937292](https://doi.org/10.1051/0004-6361/201937292)

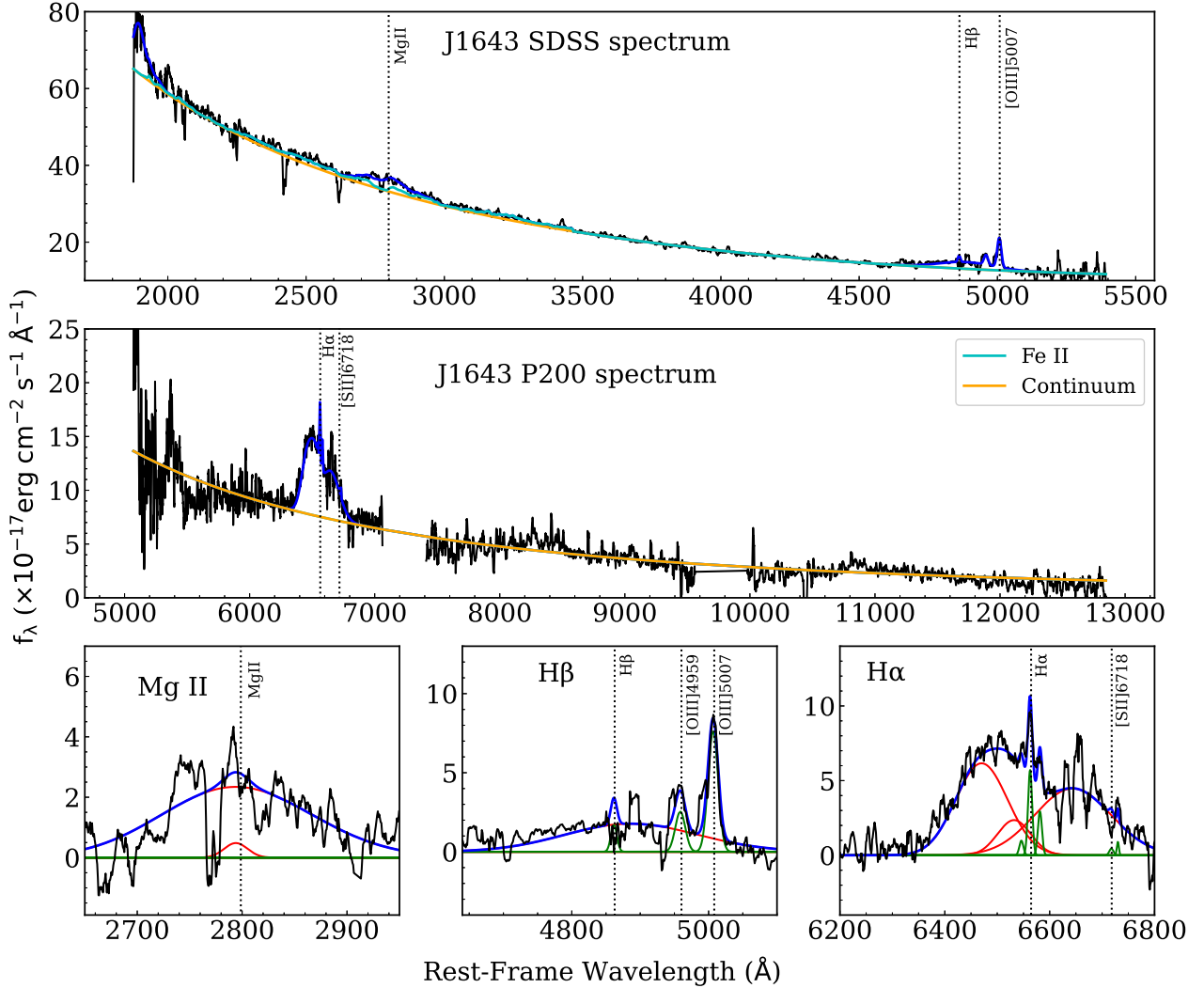


Figure A1. Similar to Figure 2 but for the SDSS and P200/TSpec spectra of SDSS J164302.03+441422.1. In the bottom panel, we show the zoomed-in view of the spectrum in the Mg II, H β , and H α regions, respectively.

APPENDIX

A. SDSS AND P200 SPECTRA OF SDSS J164302.03+441422.1

The Mg II line in the SDSS spectrum of SDSS J164302.03+441422.1 was wrongly identified as the C IV line in the SDSS DR7 quasar catalog (Shen et al. 2011), and thus the redshift of 1.650 was incorrect. The wrong redshift was fixed (updated $z = 0.917$) in the updated SDSS quasar catalog of Wu & Shen (2022). The P200/TSpec spectrum thus covers only the H α line. We fitted the SDSS and P200 spectra with the updated redshift, and the results are shown in Figure A1. The REWs of the Mg II, H β , and [O III] lines are $12.56 \pm 1.6 \text{ \AA}$, $30.4 \pm 4.6 \text{ \AA}$, and $11.56 \pm 1.6 \text{ \AA}$, respectively, which are consistent with the measurements in Wu & Shen (2022). The H β line appears very broad ($\text{FWHM} \approx 13500 \text{ km s}^{-1}$). Both the Mg II and H β lines are relatively weak; the Mg II REW is similar to the average value for the Plotkin et al. (2015) WLQ sample, and the H β REW is slightly smaller than the average value for our sample. However, the [O III] line has a typical REW compared to typical quasars (e.g., compared to the distribution in Figure 3a). Since this quasar is at a lower redshift, and it does not have measurements of the C IV line, we consider it only a WLQ candidate and did not include it in our sample.